IEEE Access
Multidisciplinary ⋮ Rapid Review ⋮ Open Access Journal

Received 4 August 2025, accepted 7 September 2025, date of publication 10 September 2025,
date of current version 19 September 2025.

Digital Object Identifier 10.1109/ACCESS.2025.3608297

RESEARCH ARTICLE

Offshore Hydrogen Production via the PEM Electrolyser Coupled With the Reverse Osmosis System

SIAVASH ASIABAN[1,2], DIMITAR BOZALAKOV[1,2], (Senior Member, IEEE), EMILE CORNELISSEN[3,4,5], AND LIEVEN VANDEVELDE[1,2], (Senior Member, IEEE)

[1]Department of Electromechanical, Systems and Metal Engineering, Faculty of Engineering and Architecture, Tech Lane Ghent Science Park, Campus Ardoyen, Ghent University, 9052 Ghent, Belgium
[2]FlandersMake@UGent—Corelab MIRO, Flanders Make, 9052 Ghent, Belgium
[3]KWR Water Research Institute, 3433 PE Nieuwegein, The Netherlands
[4]Particle and Interfacial Technology Group (PaInT), Ghent University, 9000 Ghent, Belgium
[5]Centre for Advanced Process Technology for Urban Resource Recovery (CAPTURE), 9052 Ghent, Belgium

Corresponding author: Siavash Asiaban (siavash.asiaban@ugent.be)

This work was supported by the MuSE Project funded by the Energy Transition Fund of the Belgian Federal Government managed by the Federal Public Service (FPS) Economy.

ABSTRACT Offshore production of hydrogen using seawater reverse osmosis (SWRO) and proton exchange membrane (PEM) technologies offers a promising pathway for green hydrogen generation from renewable energy sources (RESs). Realising this potential requires the integration of the SWRO unit and PEM electrolyser into a single system, with precise modelling to address the variability of RESs. Nevertheless, there are limited studies in the literature that examine a coupled SWRO-PEM electrolyser model. Therefore, in this article, an integrated SWRO-PEM electrolyser model is developed, detailing the modelling steps for each component. The models are subsequently validated against experimental data and upscaled to reflect a realistic scenario. Finally, a straightforward control method for the SWRO unit based on the electrolyser operation is suggested. The PEM electrolyser model showed an average relative error of 0.66% in static operation and 3.93% in dynamic operation. Meanwhile, the SWRO unit demonstrated an average relative error of 3.64% for water quantity and 1.48% for water quality compared to experimental results at low total dissolved solids (TDS) values, and 2.74% and 0.13% for water quantity and quality, respectively, at seawater TDS levels. Also, the control method estimated the water demand of the electrolyser with an average error of 1.20%.

INDEX TERMS PEM electrolyser, reverse osmosis, offshore hydrogen, seawater, desalination.

I. INTRODUCTION

Stemming from the depletion of fossil fuels, increasing electricity demands and substantial awareness about environmental issues, renewable energy sources (RESs) have drawn considerable attention globally. Nonetheless, the intermittency of renewables presents multiple challenges for the power system, particularly when integrating a high share of RESs into the grid [1].

The associate editor coordinating the review of this manuscript and approving it for publication was Ching-Ming Lai.

A. BACKGROUND

The production of green molecules from RESs, as an approach to accommodate their fluctuations, is one of the solutions suggested in the literatures [2], [3], and [4]. Sustainable hydrogen production via electrolysis, besides its other derivatives such as methane and methanol, enables the power system operator to balance the grid in case of a mismatch between the generation and load [5], [6], [7].

As for the required water for electrolysis, the consumption of clean water causes challenges for green hydrogen production due to the water scarcity problem. Furthermore,

freshwater is unevenly distributed around the world [8], [9]. Hence, replacing freshwater with non-clean water such as groundwater, brackish water and seawater has been investigated in the literature as an alternative [10]. Regarding the needed power for the electrolysis, offshore wind energy has demonstrated strong potential among the RESs, especially for the countries with access to the sea [11], [12]. Thus, employing offshore wind to power electrolysers has emerged as a promising option. This also offers the opportunity to place the electrolyser at sea, allowing the use of seawater as a substitute for clean water in electrolysis. Furthermore, producing hydrogen at sea is beneficial for regions with limited onshore areas. Offshore hydrogen production also allows for the integration of other marine RESs, such as wave and tidal energy [13]. Besides, it leverages the concept of the so-called energy island, which proposes locating the energy conversion and storage units along with their associated equipment at sea, such as close to offshore wind farms [14].

Nonetheless, installing electrolysers at sea introduces challenges related to their operation and maintenance and leads to higher costs, which need to be taken into account [15], [16]. Moreover, since seawater contains impurities, particularly high concentrations of Na and Cl, feeding it to electrolysers is more complicated than using clean water, as these impurities affect the lifetime and performance of electrolysers, as well as the material selection for the electrolyser and its associated systems [17], [18]. To address this issue, there are two primary methods for hydrogen production based on seawater, i.e., direct seawater electrolysis (DSWE) and seawater electrolysis with upfront water treatment. DSWE demands significant re-designing of the existing commercial electrolysers as well as the development of new electrocatalysts for both mature types of electrolyser, namely, alkaline electrolyser (AE) and proton exchange membrane (PEM) electrolysers [19]. This is because the high concentrations of corrosive chloride ions in seawater can negatively affect the durability and performance of the electrolysers, while also impacting the choice of materials used for the electrolyser. On the other hand, the upfront treatment of seawater introduces additional components and complexity to the configuration of the hydrogen production system, potentially leading to increased costs.

B. LITERATURE REVIEW

In the literature, offshore hydrogen production has been explored from various perspectives, including comparisons between DSWE and electrolysers coupled with desalination systems. These studies have also investigated the most suitable type of electrolyser and desalination system for offshore hydrogen production, deciding where to place the electrolyser onshore or offshore, and if offshore, determining the optimal location, such as integrated with a wind turbine, on a stationary platform, on a moving vessel, etc. Additionally, there are studies that have examined methods for transporting the produced hydrogen to shore and how all these factors influence the levelised cost of hydrogen (LCOH).

In this subsection, a thorough literature review is conducted to identify the most effective current topologies and pathways for offshore hydrogen production. Based on this review, the configuration considered in this study will be chosen and key areas requiring further investigations will be highlighted.

When comparing DSWE and seawater electrolysis with upfront treatment in terms of energy consumption, the electrolysis process is far more energy-intensive than water desalination. Current commercial reverse osmosis (RO) systems require around 2-4 kWh to produce 1 m^3 of ultrapure water suitable for electrolysis, whereas over 5000 kWh of energy is needed to split that same 1 m^3 of water into hydrogen and oxygen [19], [20], [21].

The authors in [19] have provided a detailed breakdown of the energy requirement, capital costs, operating costs and LCOH for a seawater reverse osmosis (SWRO) system coupled with a PEM electrolyser plant with a production capacity of 50 tons hydrogen per day. The study showed that SWRO consumes only 0.1% of the total energy required for the entire system. Additionally, the capital costs of SWRO, including its installation, make up around 3% of the total capital expenditure (CAPEX), whereas the capital costs for the electrolyser, including its installation and balance of plant (BoP) equipment, account for the remaining 97%. In terms of operational expenditure (OPEX), SWRO represents around 0.2% of the costs. Concerning the levelised cost of hydrogen, it rises marginally from 3.81 $\$/kg_{H_2}$ to 3.83 $\$/kg_{H_2}$ when SWRO is included. The authors suggested that the integration of SWRO and the PEM electrolyser is the most viable option to be utilised in the near-term applications, considering that it is a more practical immediate method than investing in developing catalysts and systems for DSWE. It is concluded that, in the SWRO-PEM system, the required energy for the electrolysis phase remains dominant compared to the SWRO process, making the capital and operating costs of the SWRO system negligible in comparison.

The authors in [22] have compared the production of 1 kg of purified water from seawater via the SWRO system and the electrolysis of that 1 kg of water from the perspectives of energy, economic and footprint. In terms of thermodynamic energy requirements, it has been shown that electrolysis requires around 3000 times more energy than desalination of seawater. Generally, electrolysis involves breaking strong covalent O-H bonds, whereas the energy for desalination is required for the reversal of entropy, overcoming the osmotic pressure which is resisting the separation of water from salt, and breaking the ion-dipole interactions between dissolved salts and water molecules. All of these energy requirements in desalination are significantly lower than breaking O-H bonds during electrolysis. Therefore, seawater desalination increases thermodynamic energy requirements

by only 0.03%. About energy consumption, with a higher heating value of 1.48 V, the voltage efficiency for acidic and alkaline electrolysers has been estimated to be 62-82%, yielding 19.38-25.63 MJ/kg_{water}. In contrast, based on the assumption of 2.5-4 kWh/m^3_{water} needed energy for seawater desalination, the energy consumption of desalination reduces to 9-14.4 kJ/kg_{water}. Consequently, electrolysis requires roughly 1350-2850 times more energy than desalination. The authors have also compared the space required by a desalination system and an electrolyser. They have estimated that desalination can produce 1000 kg of water per day per 1 m^2 of the membrane. Conversely, an electrolyser operating at 1 A/m^2 demands around 8 kg of water per day per 1 m^2 of electrochemical cell, including a gas separator, either membrane or diaphragm, and two electrodes, meaning an electrolyser needs roughly 125 times more surface area than an RO system.

As for the choice of the desalination type, membrane-based seawater desalination is recognised as one of the most practical solutions [23], [24]. Within this category, RO and forward osmosis (FO) are the most prominent technologies. RO is a pressure-driven process that relies on the difference between the applied hydraulic pressure and the osmotic pressure, the former opposing the osmotic pressure gradient. In contrast, FO employs osmotic pressure difference across the membrane as its driving force, eliminating the need for hydraulic pressure [25]. This makes RO more energy-intensive compared to FO. However, RO offers several advantages such as high reliability and high salt rejection [20]. Additionally, thanks to the development of membranes with higher efficiency, materials with lower friction and variable-frequency drives, the energy consumption of RO has decreased significantly, from 20 kWh/m^3_{water} in the 1970s to 2-3 kWh/m^3_{water} today [20]. That is why most of the current commercial desalination plants work based on the RO process, whereas FO has not yet been implemented on a large full-scale for seawater desalination.

Considering the type of electrolyser suitable for offshore use, the authors in [26] have explored seawater electrolysis technologies for offshore hydrogen production. In this study, it is shown that the differences between AE and PEM electrolysers are indeed trivial. Seeking the best current electrolysis technology to produce hydrogen at sea using marine energy, this study compared AE, PEM electrolyser, solid oxide (SO) electrolyser and DSWE based on economic, environmental and social criteria. Subsequently, five different decision-making methods are utilised to compare the mentioned hydrogen production technologies. Overall, this study concluded that both AE and PEM electrolysers are likely to play major roles in the sector of hydrogen production at sea, with PEM currently presenting the best prospects for applicability. Furthermore, the authors suggested that if AE advances to become less risky for offshore applications, it could become a more promising technology. This arises from the fact that not only AE is cheaper than PEM electrolyser but also has the longest lifespan at sea in comparison with other seawater electrolysis technologies, as it does not suffer from irreversible damage due to impurities in feed water.

The authors in [27] have conducted a techno-economic analysis of hydrogen production from an offshore wind farm, comparing both offshore and onshore production methods. Furthermore, in terms of offshore hydrogen production, they have assessed hydrogen offloading pathways to export it from an offshore facility to shore. Besides onshore hydrogen production, four pathways for offshore hydrogen production have been investigated: transporting compressed hydrogen gas to shore via pipeline, transporting liquified hydrogen to shore via vessel, converting hydrogen to ammonia (NH_3) and then transporting it to shore by either pipeline or vessel, and loading hydrogen into liquid organic hydrogen carriers (LOHC) and then transporting to shore by pipeline or vessel. Among the explored cases, producing hydrogen offshore and transporting it to shore via pipeline led to the lowest LCOH at 5.35 €/kg_{H_2}, with the potential to drop as low as 2.17 €/kg_{H_2}. Regarding onshore hydrogen production, the study suggested that onshore production is suitable if the wind farm is relatively close to land, yielding an LCOH of 5.39 €/kg_{H_2} for onshore production, with the potential to be as low as 2.61 €/kg_{H_2}.

The authors in [28] have investigated both onshore and offshore hydrogen production powered by large-scale wind turbines. In this study, three various topologies were defined as follows: placing the electrolyser onshore in remote areas and powering it using floating offshore wind turbines via submarine electric cables, locating the electrolyser on the turbine platform to avoid power transmission loss and costs, and transporting hydrogen to shore via pipelines, and finally, placing the electrolyser on a floating vessel offshore and transporting hydrogen to shore via pipelines. For each proposed topology, a comparison regarding the choice of electrolyser, floating offshore wind platform and energy transmission vector (electric power or offshore hydrogen pipelines) is made. About the first topology, the authors concluded that AE powered by a spar floating offshore wind platform is the most suitable option, with energy transmission via submarine high voltage direct current (HVDC) cables. It is important to note that in the conducted study by the authors, HVDC was investigated due to the relatively long distance between the wind farm and the electrolysers. Regarding the second topology, either the AE or PEM electrolyser is suggested with either the spar or semi-submersible offshore wind turbine, with the spar being preferred for sites with high depths, and hydrogen pipelines for transport. In terms of the third topology, they recommended the PEM electrolyser combined with semi-submersible floating offshore wind turbines and hydrogen pipelines for transport.

In [29], motivated by the construction of the artificial energy island in Denmark, the authors have assessed how to minimise the cost of green hydrogen production. In this

study, the electrolyser is powered by offshore wind energy, where three different electrolyser placements are taken into account: in-turbine, offshore and onshore. Additionally, the authors have evaluated three types of electrolysers, namely, AE, PEM and SO electrolysers, and two different operation modes, hydrogen-driven (prioritising hydrogen production) and electricity-driven (utilising only excess electricity for electrolysis). The study concluded that although all three mentioned types of electrolysers are competitive, AE achieves slightly lower costs. For electrolyser location, offshore placement yields the lowest cost of hydrogen, with the minimum LCOH in hydrogen-driven mode calculated at 2.4 €/kg_{H_2}. Finally, in electricity-driven mode, they concluded that the levelised cost of electricity (LCOE) can be reduced by up to 13% when the electrolyser is installed compared to when it is not.

On the other hand, the authors in [30] have examined offshore hydrogen production via AE, PEM and SO electrolysers powered by offshore wind power, based on the Chinese power system data. They have concluded that the PEM electrolyser is currently the most suitable electrolyser for hydrogen production. Furthermore, the study has concluded that integrating the PEM electrolyser into the wind turbine is a better solution, as it eliminates the need for submarine cables along with several power conversion and conditioning units.

To determine the most economical approach to connecting offshore wind power to electrolysers, the authors in [13] have conducted a techno-economic analysis on three various configurations, including distributed hydrogen production, centralised hydrogen production and onshore hydrogen production. In the first scenario, each wind turbine is equipped with an electrolyser, producing hydrogen on floating structures. In the centralised generation case, the electrolyser is placed on an offshore platform near the wind farm. Lastly, in the onshore production configuration, the electrolyser is located onshore. The LCOH using a PEM electrolyser coupled with a 160 MW offshore wind farm was found to be 13.81, 13.84 and 14.58 \$/kg_{H_2} for distributed, centralised, and onshore production, respectively. Additionally, a sensitivity analysis revealed that the capacity factor of the wind farm and the tax rate are the two most influential parameters in determining LCOH, followed by wind turbine costs, the electrolysis unit cost for distributed production, and floating configuration for the other two scenarios.

C. TOPOLOGY SELECTION

In summary, due to the fluctuations of RESs, new emerging concepts such as energy islands, and limited onshore areas, investigating offshore hydrogen from seawater is crucial.

Based on the conducted studies in [19] and [22], in this article, offshore hydrogen production in the presence of a desalination system is going to be explored. This is due to the negligible complexity and costs that the desalination unit adds to the topology of the system, whereas DSWE requires significant redesigns of currently available electrolysers.

For the choice of the destination system, based on the literature, the main drawback of RO compared to FO is its higher energy consumption, whereas it offers several advantages [20]. Most importantly, when integrated with an electrolyser, the higher energy consumption of RO compared to FO becomes significantly less relevant, as the specific energy consumption of RO is negligible compared to that of the electrolyser, according to [19] and [22]. Additionally, the global installed capacity for RO was around 65.5 Mm^3/day in 2019, accounting for approximately 70% of the total desalination capacity at the time. This capacity has since grown to about 100 Mm^3/day. Conversely, FO capacity has remained below 0.95 Mm^3/day, primarily limited to pilot scales operations [31], [32]. Given its maturity, the RO system is chosen for desalinating seawater to provide the feed water for the electrolyser.

Considering the conducted studies in [13], [26], [28], [29], [30], and [33], AE and PEM electrolysers are currently further along in development and more feasible solutions for near-term offshore hydrogen production. Therefore, the focus for selecting the type of electrolyser is limited to these two types.

Although AE is a more mature technology compared to its PEM counterpart, the PEM electrolyser offers several advantages over AE, particularly when it comes to integration with RESs. Firstly, the PEM electrolyser has the capability to operate at higher current densities of more than 2 A/cm^2 [34], reducing the footprint compared to AE of the same capacity. This, in turn, makes PEM electrolyser suitable for applications with limited space, such as offshore hydrogen production on an energy island. Additionally, the solid electrolyte of the PEM electrolyser allows for faster response times compared to AE, where a liquid electrolyte is utilised, resulting in higher inertia, and thus, more sluggish ion transportation [35], [36]. This rapid response is crucial when connected to an intermittent RES, as the electrolyser needs to operate under fast dynamics. Consequently, due to its maturity, AE is mainly employed in fixed-power applications [37]. Conversely, the PEM electrolyser is preferred for integration with renewables since it can start up in several minutes and ramp up from idle mode to rated power in just a few seconds [35]. Moreover, the PEM electrolyser not only has higher efficiency compared to AE but also is capable of operating under a wider range of current densities, making it a more suitable choice for providing ancillary services for the electricity grid when coupled with RESs [38], [39].

Thus, in this article, the PEM electrolyser is selected for offshore hydrogen production coupled with the RO desalination system.

Although numerous studies have indicated that coupling RO with either AE or PEM electrolyser has the highest potential for near-future offshore hydrogen production, there

are few studies in the literature that examine the integrated operation of these units. Since the costs and energy consumption of water treatment are lower compared to the overall hydrogen production system, it is often overlooked, despite being an essential component of the system. Therefore, a coupled model of the PEM electrolyser and RO system, as the two most promising technologies for offshore hydrogen production from seawater, is necessary for further studies.

Whereas it is certainly valid that the consumed energy, added costs and footprint of the RO system are negligible compared to the electrolyser, hydrogen production with upfront water treatment is only deemed acceptable and competitive to DSWE if only it is ensured that the feed water for the electrolyser meets the minimum requirement in terms of quantity and quality [19].

In the context of the SWRO-PEM topology, in [40], the authors have explored an off-grid offshore PEM electrolyser and RO system powered by wave energy. The model also includes battery storage systems and compression units for hydrogen storage. Furthermore, a simple energy management strategy is proposed to operate the components based on the available energy, battery state of charge and water availability. Although wave energy is less fluctuating compared to offshore wind, the dynamic behaviour of the PEM electrolyser is not accounted for, which impacts the accuracy of results. Consequently, the consumed power by the electrolyser, and thus the amount of hydrogen produced, is overestimated. Additionally, the behaviour of the RO system, and hence the quality and quantity of feed water for the electrolyser, is not explored. This omission hinders the proper sizing of the RO system, which is of paramount importance when electrolysis with upfront treatment is considered.

The authors in [41] have compared the water demands and operating costs for a solar-powered electrolyser supplied with desalinated seawater which is produced through either RO or low-temperature multi-effect distillation. They found that the costs associated with the latter are up to 85% lower than those for RO, and that the electrolyser coupled with low-temperature multi-effect distillation exhibited lower water demands. These advantages are attributed to the elimination of the need to install and operate cooling towers in low-temperature multi-effect distillation. Nevertheless, the study has primarily focused on waste heat management, and an integrated model of the electrolyser with either RO or distillation has not been in the scope of their research. Furthermore, although the desalination process costs affect the levelised cost of water (LCOW), they have a negligible influence on the LCOH when considered as a single system.

Hence, in this study, an SWRO-PEM model is developed and coupled into a single system-level simulation, unlocking several opportunities for further studies in the field of offshore hydrogen production from non-fresh water sources.

The rest of the article is structured as follows: Section II provides a detailed description of the PEM electrolyser model, previously developed by the authors [42], followed by its validation. Section III outlines the modelling approach for the RO system and its validation against experimental data. Thereafter, in Section IV, the validated models are first upscaled and then coupled, with a computationally efficient control method introduced to adjust the setting of the RO unit based on the energy consumption of the PEM electrolyser. Finally, Section V discusses the conclusions and highlights potential areas for future research.

II. PEM ELECTROLYSER MODEL

In an SWRO-PEM model, the electrolyser is the dominant energy-consuming component. Therefore, in this article, a dynamic model has been developed to accurately predict power consumption and hence hydrogen production.

A. PEM ELECTROLYSER MODEL DESCRIPTION

As for the PEM electrolyser, pure water is introduced to the anode, where the applied current splits it into hydrogen protons, electrons and oxygen. This is known as the oxidation reaction, as indicated in (1). Thereafter, the electrons move through the electric circuit towards the cathode, while hydrogen ions migrate through the membrane and reach the cathode as well. This process is referred to as the reduction reaction, as shown in (2). The overall process, known as the redox reaction, is illustrated in (3).

$$2H_2O \rightarrow 4H^+ + 4e^- + O_2 \tag{1}$$

$$4H^+ + 4e^- \rightarrow 2H_2 \tag{2}$$

$$2H_2O \rightarrow 2H_2 + O_2 \tag{3}$$

whereas the anode and cathode ancillaries are modelled based on the molar balances of their associated substances – water and oxygen for the anode, and water and hydrogen for the cathode – the membrane module simulates the mechanisms by which water traverses it. This model considers electro-osmotic drag and diffusion as the primary methods of water transport through the membrane. In the voltage module, besides the reversible voltage calculations, the main overvoltages occurring in the PEM electrolyser are modelled, specifically the ohmic overvoltage of the membrane and the activation overvoltages of the anode and cathode. Lastly, the thermal module includes the heat sources and sinks in the PEM electrolyser.

The equations utilised for developing the PEM electrolyser model are shown in Table 1 and Table 2.

1) ANODE MODULE

Considering the anode, (4) and (5) describe the molar balance equations of water and oxygen at the anode, respectively. Here, $\dot{N}_{H_2O_{an,in}}$ and $\dot{N}_{H_2O_{an,out}}$ represent the anode inlet and outlet molar flow rates of water, whereas $\dot{N}_{O_{2an,in}}$ and $\dot{N}_{O_{2an,out}}$ are the anode inlet and outlet molar flow rates of oxygen at the anode. Besides, $\dot{N}_{H_2O_{an,cons}}$ corresponds to the molar flow rate of the consumed water at the anode, $\dot{N}_{H_2O_{mem}}$ stands for the molar flow rate of the water passage from the anode to

TABLE 1. Equations used for modelling of the PEM electrolyser - Part 1.

No.	Equation	Module	Reference
(4)	$\dot{N}_{H_2O_{an}} = \dot{N}_{H_2O_{an,in}} - \dot{N}_{H_2O_{an,cons}} - \dot{N}_{H_2O_{mem}} - \dot{N}_{H_2O_{an,out}}$	Anode	[43]
(5)	$\dot{N}_{H_2O_{an}} = \dot{N}_{H_2O_{an,in}} - \dot{N}_{H_2O_{an,cons}} - \dot{N}_{H_2O_{mem}} - \dot{N}_{H_2O_{an,out}}$	Anode	[43]
(6)	$\dot{N}_{H_2O_{an,cons}} = \frac{nI}{2F}$	Anode	[44]
(7)	$\dot{N}_{O_{2an,gen}} = \frac{nI}{4F}$	Anode	[44]
(8)	$p_{H_2O_{an}} = \frac{N_{H_2O_{an}} R_u T}{v_{an}}$	Anode	[43]
(9)	$p_{O_{2an}} = \frac{N_{O_{2an}} R_u T}{v_{an}}$	Anode	[43]
(10)	$P_{an} = p_{H_2O_{an}} + p_{O_{2an}}$	Anode	[43]
(11)	$X_{H_2O_{an}} = \frac{p_{H_2O_{an}}}{P_{an}}$	Anode	[45]
(12)	$X_{O_{2an}} = \frac{p_{O_{2an}}}{P_{an}}$	Anode	[45]
(13)	$\dot{N}_{H_2O_{ca}} = \dot{N}_{H_2O_{ca,in}} + \dot{N}_{H_2O_{mem}} - \dot{N}_{H_2O_{ca,out}}$	Cathode	[45]
(14)	$\dot{N}_{H_{2ca}} = \dot{N}_{H_{2ca,in}} + \dot{N}_{H_{2ca,gen}} - \dot{N}_{H_{2ca,out}}$	Cathode	[45]
(15)	$\dot{N}_{H_{2ca,gen}} = \frac{nI}{2F}$	Cathode	[44]
(16)	$p_{H_2O_{ca}} = \frac{N_{H_2O_{ca}} R_u T}{v_{ca}}$	Cathode	[43]
(17)	$p_{H_{2ca}} = \frac{N_{H_{2ca}} R_u T}{v_{ca}}$	Cathode	[43]
(18)	$P_{ca} = p_{H_2O_{ca}} + p_{H_{2ca}}$	Cathode	[43]
(19)	$X_{H_2O_{ca}} = \frac{p_{H_2O_{ca}}}{P_{ca}}$	Cathode	[45]
(20)	$X_{H_{2ca}} = \frac{p_{H_{2ca}}}{P_{ca}}$	Cathode	[45]
(21)	$\dot{N}_{H_2O_{mem}} = \dot{N}_{H_2O_{mem,eod}} + \dot{N}_{H_2O_{mem,diff}} - \dot{N}_{H_2O_{mem,hp}}$	Membrane	[35]
(22)	$\dot{N}_{H_2O_{mem,eod}} = \frac{n_d j A}{F}$	Membrane	[35]
(23)	$n_d = -2.89556 + 0.016T$	Membrane	[46]
(24)	$\dot{N}_{H_2O_{mem,diff}} = \frac{AD_w}{\delta_{mem}}(C_{H_2O_{mem,cat}} - C_{H_2O_{mem,an}})$	Membrane	[35]
(25)	$D_w = D'_w \exp\left[2416\left(\frac{1}{303} - \frac{1}{T}\right)\right]$	Membrane	[43]
(26)	$D'_w = \begin{cases} 10^{-10}\lambda_{mem} & \lambda_{mem} < 2 \\ 10^{-10}[1 + 2(\lambda_{mem} - 2)] & 2 \le \lambda_{mem} < 3 \\ 10^{-10}[3 - 1.67(\lambda_{mem} - 3)] & 3 \le \lambda_{mem} < 4.5 \\ 1.25 \times 10^{-10} & \lambda_{mem} \ge 4.5 \end{cases}$	Membrane	[43]
(27)	$\lambda_{mem} = 0.08533.T - 6.77632$	Membrane	[47]
(28)	$C_{H_2O_{mem,an}} = C_{H_2O_{ch,an}} - \frac{\delta_{an}\dot{n}_{H_2O,an}}{D_{eff,an}}$	Membrane	[35]
(29)	$C_{H_2O_{mem,ca}} = C_{H_2O_{ch,ca}} + \frac{\delta_{ca}\dot{n}_{H_2O,ca}}{D_{eff,ca}}$	Membrane	[35]
(30)	$C_{H_2O_{ch,an}} = C_{H_2O_{ch,ca}} = \frac{\rho_{H_2O_T}}{M_{H_2O}}$	Membrane	[35]
(31)	$\dot{n}_{H_2O,an} = \frac{\dot{N}_{H_2O_{mem}} + \dot{N}_{H_2O_{an,cons}}}{A}$	Membrane	[35]
(32)	$\dot{n}_{H_2O,ca} = \frac{\dot{N}_{H_2O_{ca}}}{A}$	Membrane	[35]
(33)	$\frac{1}{D_{eff,an}} = \frac{\epsilon}{\xi}\left(\frac{1}{D_{eff,O_2-H_2O}} + \frac{1}{D_{eff,H_2O-k}}\right)$	Membrane	[48]

the cathode through the membrane, and $\dot{N}_{O_{2an,gen}}$ is the molar flow rate of the produced oxygen at the anode. It should be noted that in this model, the inlet molar flow rate of oxygen at the anode is assumed to be zero, included only to maintain a comprehensive molar balance equation.

The molar flow rates of water consumption and oxygen generation at the anode can be calculated using (6) and (7), respectively. In these equations, n is the number of cells in the electrolyser, I represents the current, and F refers to the Faraday constant.

The partial pressures of water and oxygen at the anode can be determined via the ideal gas law, as shown in (8) and (9), consecutively, using (4)-(7), and solving the algebraic loops. Here, $N_{H_2O_{an}}$ and $N_{O_{2an}}$ are the number of moles of water and oxygen at the anode, R_u indicates the universal gas constant, T is the operating temperature of the electrolyser, and v_{an} denotes the anode volume. Based on (10), which provides the pressure at the anode, the molar fractions of water and oxygen at the anode are then derived via (11) and (12), respectively.

2) CATHODE MODULE

A similar approach is applied to the cathode as with the anode. Within the cathode module, (13) and (14) describe the molar flow rates of water and hydrogen at the cathode, respectively. In these equations, $\dot{N}_{H_2O_{ca,in}}$ and $\dot{N}_{H_2O_{ca,out}}$ represent the inlet

and outlet molar flow rates of water at the cathode, $\dot{N}_{H_{2ca,in}}$ and $\dot{N}_{H_{2ca,out}}$ indicate the inlet and outlet molar flow rates of hydrogen at the cathode, and $\dot{N}_{H_{2ca,gen}}$ stand for the molar rate of the generated hydrogen at the cathode. In the developed model, both the inlet hydrogen and water flow rates to the cathode are assumed to be zero.

Then, the molar flow rate of the hydrogen produced at the cathode can be determined using (15).

By applying the ideal gas law, the partial pressures of water and hydrogen at the cathode can be calculated using (16) and (17), consecutively, where $N_{H_2O_{ca}}$ and $N_{H_{2ca}}$ denote the number of water and hydrogen moles at the cathode, successively, and v_{ca} is the cathode volume. Lastly, by considering the pressure at the cathode as shown in (18), the molar fractions of water and hydrogen can be derived using (19) and (20), respectively.

3) MEMBRANE MODULE

Concerning the membrane, although a significant portion of the water participates in the oxygen evolution reaction, a part of it migrates through the membrane, affecting the performance of the electrolyser. There are three primary mechanisms which lead to the water passage through the membrane, namely, electro-osmotic drag ($\dot{N}_{H_2O_{mem,eod}}$), diffusion ($\dot{N}_{H_2O_{mem,diff}}$), and hydraulic pressure effect ($\dot{N}_{H_2O_{mem,hp}}$), as described in (21). The first two mechanisms mentioned in (21) cause water to move from the anode to the cathode, whereas the hydraulic pressure effect leads to the water passage from the cathode to the anode. Among the water passage mechanisms, electro-osmotic drag is the dominant mechanism, whereas the hydraulic pressure is negligible compared to the two other terms [43], [49]. Electro-osmotic drag can be derived using (22), where j is the current density and A represents the active area of the cell. The term n_d stands for the electro-osmotic drag coefficient, quantifying the number of water molecules dragged from the anode to the cathode per proton (mol[H_2O]/mol[H^+]). This coefficient can be empirically determined via (23) where a linear fit of n_d is provided as a function of temperature in Kelvin.

Diffusion occurs due to the concentration gradient between the anode and cathode, which can be expressed by integrating Fick's law of diffusion between the anode and cathode sides of the membrane interfaces, as shown in (24). In this equation, D_w is the diffusion coefficient, δ_{mem} represents the membrane thickness and $C_{H_2O_{mem,cat}}$ and $C_{H_2O_{mem,an}}$ are the water concentrations on the cathode and anode sides of the membrane, successively. The diffusion coefficient is determined by substituting (26) into (25), where D'_w indicates the diffusion coefficient at the reference temperature, and λ_{mem} represents the water content of the membrane, which can be empirically derived via (27). The water concentrations on the anode and cathode sides of the membrane can be calculated using (28) and (29), respectively. In these equations, $C_{H_2O_{ch,an}}$ and $C_{H_2O_{ch,ca}}$ represent the water concentrations in the anode and cathode channels, δ_{an} and δ_{ca} indicate the electrode thicknesses, and $\dot{n}_{H_2O,an}$ and $\dot{n}_{H_2O,ca}$ are the molar fluxes of water through the anode and cathode. Also, the effective binary diffusion coefficient at the anode (O_2-H_2O) and cathode (H_2-H_2O) are denoted by $D_{eff,an}$ and $D_{eff,ca}$, consecutively.

The water concentrations in the anode and cathode channels can be derived using (30), where ρ_{H_2O} is the water density at temperature T, and M_{H_2O} stands for the molar mass of water. The molar fluxes through the anode and cathode are quantified in (31) and (32), respectively. After that, the effective binary coefficients of the anode and cathode are quantified in (33) and (34), where D_{eff,O_2-H_2O} and D_{eff,H_2-H_2O} are effective molecular diffusion coefficients for the O_2-H_2O and H_2-H_2O binary systems, which reflect the molecular diffusion mechanism. Furthermore, D_{eff,H_2O-k}, the effective Knudsen diffusion coefficient for water, accounts for the Knudsen diffusion effect on the rate of water flow through the membrane. Lastly, ϵ is the electrode porosity, and ξ denotes tortuosity. Since the molecules frequently collide with the walls of the pores, the effective Knudsen diffusion coefficient is calculated using kinetic theory, as shown in (35), where r is the mean pore radius.

To calculate D_{eff,O_2-H_2O} and D_{eff,H_2-H_2O}, the Chapman-Enskog theory of the ideal gases is applied, where $\Theta_{O_2-H_2O}$ and $\Theta_{H_2-H_2O}$ indicate the mean molecular radii of the relevant substances, Ω stands for the dimensionless diffusion collision integral, and M_{O_2} and M_{H_2} are the molar masses of oxygen and hydrogen, successively. To calculate $\Theta_{O_2} - H_2O$ and $\Theta_{H_2-H_2O}$, (38) and (39) can be utilised, where Ω_D is the diffusion collision integral, which can be derived via (40). The dimensionless temperature τ is determined using (41) and (42). In these equations, $\varepsilon_{O_2-H_2O}$ and $\varepsilon_{H_2-H_2O}$ are the Lennard-Jones energies, which can be obtained using (43) and (44). Finally, the total water passage through the membrane can be calculated using (45).

4) VOLTAGE MODULE

In electrolysis, a minimum voltage is required to initiate the process, referred to as the reversible voltage. Nevertheless, due to the voltage drops within the electrolyser, a higher voltage needs to be applied in practice. The total cell voltage, which is shown in (46), comprises the reversible cell voltage (V_{rev}), activation overvoltage (V_{act}), ohmic overvoltage (V_{ohm}), and concentration overvoltage (V_{con}).

Concentration overvoltage occurs when oxygen and hydrogen accumulate in the catalyst layers of the anode and cathode. However, when the flow field effectively facilitates gas removal, the concentration overvoltage becomes insignificant [43]. Also, for current densities below 3 A/cm^2, the activation and ohmic overvoltages are significantly higher than the concentration overvoltage [43], [59], [60]. Given the considered operating condition in this study, as discussed in Section IV, concentration overvoltage is neglected in this article.

TABLE 2. Equations used for modelling of the PEM electrolyser - Part 2.

No.	Equation	Module	Reference
(34)	$\frac{1}{D_{\text{eff,ca}}} = \frac{\epsilon}{\xi}\left(\frac{1}{D_{\text{eff},H_2-H_2O}} + \frac{1}{D_{\text{eff},H_2O-k}}\right)$	Membrane	[48]
(35)	$D_{\text{eff},H_2O-k} = \frac{4}{3} r \sqrt{\frac{8R_uT}{\pi M_{H_2O}}}$	Membrane	[50]
(36)	$D_{\text{eff},O_2-H_2O} = 0.00133 \frac{T^{3/2}}{P_{\text{an}}\Theta^2_{O_2-H_2O}\Omega_D}\sqrt{\frac{1}{M_{O_2}} + \frac{1}{M_{H_2O}}}$	Membrane	[50]
(37)	$D_{\text{eff},H_2-H_2O} = 0.00133 \frac{T^{3/2}}{P_{\text{ca}}\Theta^2_{H_2-H_2O}\Omega_D}\sqrt{\frac{1}{M_{H_2}} + \frac{1}{M_{H_2O}}}$	Membrane	[50]
(38)	$\Theta_{O_2-H_2O} = \frac{\Theta_{O_2}+\Theta_{H_2O}}{2}$	Membrane	[35]
(39)	$\Theta_{H_2-H_2O} = \frac{\Theta_{H_2}+\Theta_{H_2O}}{2}$	Membrane	[35]
(40)	$\Omega_D = \frac{1.06}{\tau^{0.156}} + \frac{0.193}{\exp(0.76\tau)} + \frac{1.036}{\exp(1.53\tau)} + \frac{1.765}{3.894\tau}$	Membrane	[50]
(41)	$\tau_{O_2-H2O} = \frac{kT}{\varepsilon_{O_2-H_2O}}$	Membrane	[50]
(42)	$\tau_{H_2-H2O} = \frac{kT}{\varepsilon_{H_2-H_2O}}$	Membrane	[50]
(43)	$\varepsilon_{O_2-H_2O} = \sqrt{\varepsilon_{O_2}\varepsilon_{H_2O}}$	Membrane	[50]
(44)	$\varepsilon_{H_2-H_2O} = \sqrt{\varepsilon_{H_2}\varepsilon_{H_2O}}$	Membrane	[50]
(45)	$\dot{N}_{H_2O_{\text{mem}}} = \frac{AD_w}{\delta_{\text{mem}}}\left[\left(\frac{\rho_{H_2O_T}}{M_{H_2O}} + \frac{\delta_{\text{ca}}\dot{n}_{H_2O,\text{ca}}}{D_{\text{eff,ca}}}\right) - \left(\frac{\rho_{H_2O_T}}{M_{H_2O}} - \frac{\delta_{\text{an}}\dot{n}_{H_2O,\text{an}}}{D_{\text{eff,an}}}\right)\right] + \frac{n_d jA}{F}$	Membrane	[35]
(46)	$V_{\text{cell}} = V_{\text{rev}} + V_{\text{act}} + V_{\text{ohm}} + V_{\text{con}}$	Voltage	[35]
(47)	$V_{\text{rev}} = E_0 + \frac{R_uT}{2F}\ln(\frac{p_{H2}\sqrt{pO2}}{p_{H_2O}})$	Voltage	[51]
(48)	$E_0 = 1.229 - 0.9\times10^{-3}(T-298)$	Voltage	[51]
(49)	$V_{\text{act}} = V_{\text{act,an}} + V_{\text{act,ca}}$	Voltage	[52]
(50)	$V_{\text{act,an}} = \frac{R_uT}{\alpha_{\text{an}}F}\text{arcsinh}(\frac{j}{2j_{0,\text{an}}})$	Voltage	[52]
(51)	$V_{\text{act,ca}} = \frac{R_uT}{\alpha_{\text{ca}}F}\text{arcsinh}(\frac{j}{2j_{0,\text{ca}}})$	Voltage	[52]
(52)	$j_{0,\text{an}} = j_{0,\text{an-ref}}\exp[-\frac{E_{\text{act}}}{R_u}(\frac{1}{T} - \frac{1}{T_{\text{ref}}})]$	Voltage	[53]
(53)	$j_{0,\text{ca}} = j_{0,\text{ca-ref}}\exp[-\frac{E_{\text{act}}}{R_u}(\frac{1}{T} - \frac{1}{T_{\text{ref}}})]$	Voltage	[53]
(54)	$R_{\text{ohm},i} = \frac{\delta_{\text{mem}}}{\sigma_{\text{mem}}}$	Voltage	[54]
(55)	$\sigma_{\text{mem}} = (0.514\lambda_{\text{mem}} - 0.326).\exp[1268(\frac{1}{303} - \frac{1}{T})]$	Voltage	[43]
(56)	$V_{\text{ohm}} = R_{\text{ohm,i}} \times j$	Voltage	[53]
(57)	$C_{\text{l,stack}} = \sum_k c_{\text{p,k}}\nu_k.\rho_k$	Thermal	[53]
(58)	$C_{\text{l,stack}}\frac{dT}{dt} = Q_{\text{gen}} + \sum_k \dot{M}_{\text{in,k}}c_{\text{p,k}}T_{\text{in}} - Q_{\text{loss}} - Q_{\text{cool}} - \sum_k \dot{M}_{\text{out,k}}c_{\text{p,k}}T_{\text{out}}$	Thermal	[55]
(59)	$\dot{M}_{\text{in},H_2O,\text{an}} = (1+\Lambda_{H_2O})M_{H_2O}\frac{I}{2F}$	Thermal	[56]
(60)	$\dot{M}_{\text{in},H_2O,\text{ca}} = \Lambda_{H_2O}M_{H_2O}\frac{I}{2F}$	Thermal	[56]
(61)	$\dot{M}_{\text{out},H_2O,\text{an}} = \dot{M}_{\text{out},H_2O,\text{ca}} = \Lambda_{H_2O}M_{H_2O}\frac{I}{2F}$	Thermal	[56]
(62)	$\dot{M}_{\text{out},O_2,\text{an}} = M_{O_2}\frac{I}{4F}$	Thermal	[56]
(63)	$\dot{M}_{\text{out},H_2,\text{ca}} = M_{H_2}\frac{I}{2F}$	Thermal	[56]
(64)	$Q_{\text{gen}} = \left(V_{\text{cell}} - \frac{\Delta H}{2F}\right)I$	Thermal	[56]
(65)	$\Delta H(T,p) = \Delta H_{H_2} + \frac{1}{2}\Delta H_{O_2} - \Delta H_{H_2O}$	Thermal	[57]
(66)	$\widehat{\Delta H_k} = \widehat{\Delta H_k^0} + c'_{\text{p}}(T - T_0)$	Thermal	[57]
(67)	$Q_{\text{loss}} = hA_{st}(T - T_{\text{amb}})$	Thermal	[58]
(68)	$\Lambda_{H_2O} = \frac{F}{M_{H_2O}.c_{p,H_2O}.\Delta T}\left(V_{\text{cell}} - \frac{\Delta H}{2F}\right)$	Thermal	[55]

The reversible voltage can be quantified using the Nernst equation, as shown in (47). Because the reversible voltage depends on the operating conditions of the electrolyser, such as pressure and temperature, the second term in (47) indicates its deviation from the standard value under different conditions. The standard reversible voltage, E_0, can be empirically expressed as a function of temperature, as illustrated in (48).

The activation overvoltage refers to the required voltage to drive the electrochemical reactions at the anode and cathode, described in (49). This overvoltage accounts for the energy losses resulting from the charge transfer kinetics within the electrolyser. Employing the Butler-Volmer equation, the activation overvoltage at the anode and cathode can be determined with (50) and (51), respectively. In these equations, α_{an} and α_{ca} represent the charge transfer coefficients, and $j_{0,\text{an}}$ and $j_{0,\text{ca}}$ are the exchange current densities of the anode and cathode, successively. Given the wide range of reported values for these four parameters in the literature, they are treated as fitting parameters in this article, similar to some other studies such as [35]. Additionally, the temperature dependency of the exchange current densities at the anode and cathode is expressed in (52) and (53), successively, where E_{act} indicates the activation energy of the electrodes, and $j_{0,\text{an-ref}}$ and $j_{0,\text{ca-ref}}$ are the reference exchange current densities of the anode and cathode at the reference temperature T_{ref}.

The ohmic overvoltage in the PEM electrolyser arises from various sources, which can be categorised into two types. The

first is ionic ohmic overvoltage which is related to membrane resistance, and the second is electronic ohmic overvoltage, which arises from electronic parts including bipolar plates, electrodes, etc. Since the conductivity of the membrane is considerably lower than that of the electronic components, ionic ohmic overvoltage is the dominant term [51], [55]. Thus, in this article, the electronic contribution to the ohmic voltage is neglected. Additionally, due to the short and uniform ionic conduction path in the PEM electrolyser, ionic resistance can be quantified by assuming a constant resistivity, as illustrated in (54), where σ_{mem} is the membrane conductivity in S.m^{-1}, as described in (55). Lastly, the ohmic overvoltage is calculated using (56).

5) THERMAL MODULE

The PEM electrolyser benefits from a fast response during dynamic operation, though it is not instantaneous. To effectively simulate the dynamic response of the PEM electrolyser, it is essential to include a thermal module to account for the thermal inertia of the electrolyser.

In this model, the cell temperature is considered to be homogenous and is treated as a lumped thermal capacity, as expressed in (57), where $C_{\text{l,stack}}$ represents the lumped thermal capacitance of the stack, $c_{\text{p,k}}$ indicates the specific heat, v_{k} is volume and ρ_{k} shows the density of species $k = \{H_2O, O_2, H_2\}$. Considering both the inlet and outlet flows in the electrolyser, the stack enthalpy can be calculated as shown in (58). Here Q_{gen} is the generated heat from the electrical work performed in the electrolyser, $\dot{M}_{\text{in,k}}$ and $\dot{M}_{\text{out,k}}$ show the inlet and outlet flow rates of the substance k, Q_{loss} denotes the heat exchanged between the electrolyser and the environment, Q_{cool} is the heat extracted by the coolant, and T_{in} and T_{out} are the inlet and outlet temperatures, successively. In (58), T_{in} is the known temperature of the inlet water, whereas T_{out}, the outlet temperature, can be derived by solving the equation. Moreover, the operating temperature of the electrolyser is assumed to be the average of the inlet and outlet temperatures.

Cooling the electrolyser is of significant importance. Mainly dictated by the thermal stability of perfluoro-sulfonic acid (PFSA) materials utilised as polymer electrolytes in the PEM electrolyser, it is crucial to keep the stack temperature below a threshold, typically 80 °C. Additionally, the formation of temperature gradients within the cell is undesirable because they can accelerate the ageing rate of the electrolyser and lead to non-homogenous cell loading, which negatively impacts the performance of the PEM electrolyser [61], [62].

For offshore hydrogen production, using an excess amount of water for cooling purposes is a promising approach. In this article, the required amount of water and the thermal inertia of the electrolyser are modelled by controlling the temperature difference between the inlet and outlet flows, ΔT, to avoid the appearance of a temperature gradient within the cell. To this end, by introducing the parameter Λ_{H_2O}, which quantifies the ratio of the actual water flow through the PEM electrolyser to every mole of water consumed for electrolysis, the needed amount of water is calculated. It is important to note that this excess water does not need to be supplied for each mole of water used in electrolysis, as it is recirculated within the electrolyser.

To determine the mass flow rate of the inlet flows at the anode and cathode, (59) and (60) can be utilised. On the other hand, (61)-(63) are used for the calculation of outlet mass flow rates at the anode and cathode, where M is the molar mass of the respective substance.

To quantify the amount of heat produced due to the work done in the electrolyser, (64) is utilised, where ΔH represents the total reaction enthalpy, which is described in (65) in terms of the enthalpy of the relevant substances. The enthalpy of each substance is derived using (66), where c'_{p} indicates the specific heat capacity, and $\widehat{\Delta H_k^0}$ represents the standard enthalpy of the substance k at the reference pressure and temperature of P_0 and T_0, respectively.

Finally, the heat loss exchange between the electrolyser and the environment, in the absence of insulation, can be calculated using (67). In this equation, h stands for the heat transfer coefficient, A_{st} indicates the outside surface area of the stack and T_{amb} is the ambient temperature. However, in (58), the other terms on the right-hand side have a more dominant impact on the operating temperature of the cell than Q_{loss}. Thus, in this article, Q_{loss} is neglected when calculating thermal inertia.

B. PEM ELECTROLYSER MODEL VALIDATION

To validate the accuracy of the developed model for the PEM electrolyser, the results obtained from the Matlab/Simulink simulations are compared with the set of experimental data reported in [63] and [64]. The use of different sources for static and dynamic validation is due to the absence of a single study that reports both static and dynamic responses for the same PEM electrolyser. Furthermore, each of these references offers data under various operating conditions for static and dynamic modes, which enables a comprehensive assessment of the accuracy of the model across different operational scenarios. In this section, the static response of the model is first validated at different operating temperatures using the polarisation curves from [63], with the thermal module excluded in static operation. Thereafter, the dynamic response of the model at various current densities is validated against the experimental data from [64], where the thermal module is considered in the simulations.

1) STATIC MODE

The utilised parameters used for the validation of the model are summarised in Table 3.

As previously mentioned, the four parameters $j_{0,\text{an-ref}}$, $j_{0,\text{ca-ref}}$, α_{an} and α_{ca} were treated as fitting parameters. First, the feasible ranges for the fitting parameters were determined based on the reported values in the literature.

TABLE 3. Specifications of the PEM electrolyser used for the static validation [63].

Parameter	Value	Unit
Anode material	Pt-Ir	-
Cathode material	Pt	-
Membrane	Nafion 1110	-
A	100	cm^2
F	96485.33	A.s/mol
M_{H_2}	0.002	kg/mol
M_{H_2O}	0.018	kg/mol
M_{O_2}	0.032	kg/mol
n	1	-
P_{an-ca}	1	bar
R_u	8.31	J/K.mol
T_{in}	80	°C
δ_{an-ca}	0.08	mm
δ_{mem}	0.254	mm
ϵ	0.3	-
ε_{H_2}/k	59.7	K
ε_{H_2O}/k	809.1	K
ε_{O_2}/k	106.7	K
Θ_{H_2}	2.827	Å
Θ_{H_2O}	2.641	Å
Θ_{O_2}	3.467	Å
ξ	4	-

TABLE 4. Fitted parameters for static validation.

Parameter	Considered range	Fitted value	Unit
$j_{0,an-ref}$	$10^{-11} - 10^{-4}$	2.00×10^{-8}	A/cm^2
$j_{0,ca-ref}$	$10^{-6} - 10^{-1}$	1.91×10^{-2}	A/cm^2
α_{an}	0.4 – 2.5	2.47	-
α_{ca}	0.1 – 1	0.93	-

Then, the combinations in which either $j_{0,an-ref} > j_{0,ca-ref}$ or $\alpha_{an} < \alpha_{ca}$ were excluded from the search space as typical values for these parameters follow the opposite trend. This is because the contribution of the anode to the activation overvoltage is more significant than that of the cathode. Next, the four parameters were allowed to vary in their associated feasible ranges, and the best set of combinations of the four parameters, resulting in the lowest error compared to the experimental data, was chosen. The selected ranges as well as the final chosen values of the fitting parameters are listed in Table 4. Lastly, the four chosen parameters were held constant, while varying the operating temperature to ensure that the model is valid under different operating conditions.

To identify the best combination, the relative error between the results of the model and the experimental data was calculated, and the set with the lowest error was chosen. The expression used for the relative error in percentage can be given as:

$$e = \frac{100}{Z_{exp}} \sum_{z=1}^{Z_{exp}} \frac{V_{sim,z} - V_{exp,z}}{V_{exp,z}}, \quad (4)$$

where Z_{exp} represents the number of experiments, and $V_{sim,z}$ and $V_{exp,z}$ are the results obtained from the z^{th} simulation and experiment, successively.

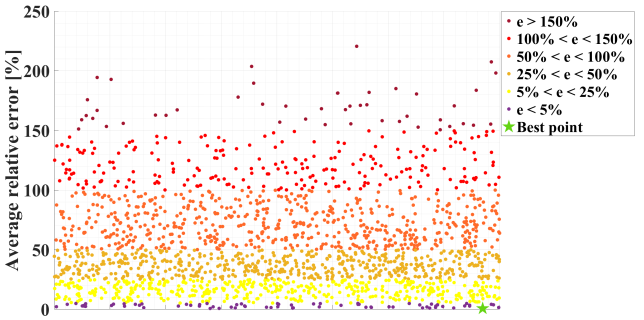

FIGURE 1. The average relative error derived from various combinations of the fitting parameters for static validation.

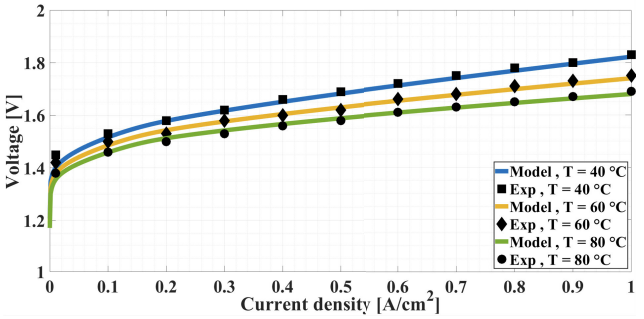

FIGURE 2. Comparison of the polarisation curves obtained from the best point of the model and experiment at various temperatures and atmospheric pressure.

The relative errors derived for various parameter combinations are depicted in Fig. 1. The case at 80 °C was chosen as the reference scenario since it is a common operating temperature for the PEM electrolyser. As shown in Fig. 1, the minimum error obtained was 0.55% for the selected set mentioned in Table. 4. Considering the materials employed for the electrodes – Pt-Ir for the anode and Pt for the cathode – the chosen set is valid [52], [65].

Keeping the chosen set of fitting parameters at 80 °C unchanged, the operating temperature was lowered to 60 °C and 40 °C to ensure that the model still holds validity. The polarisation curves generated by the developed model, along with the experimental results are presented in Fig. 2. As can be seen, the static response of the model closely matches the experimental results, with relative errors of 0.68%, 0.75% and 0.55% for the operating temperatures of 40 °C, 60 °C and 80 °C, respectively, resulting in an average relative error of 0.66% for the investigated cases.

The discrepancy between the model and experimental results can be attributed to overlooked factors such as concentration overvoltage and electronic resistance. Additionally, the higher error observed at 40 °C, 60 °C compared to the reference case is mainly because the fitting parameters were at their optimal for the reference case, which may not be optimal for other operating temperatures.

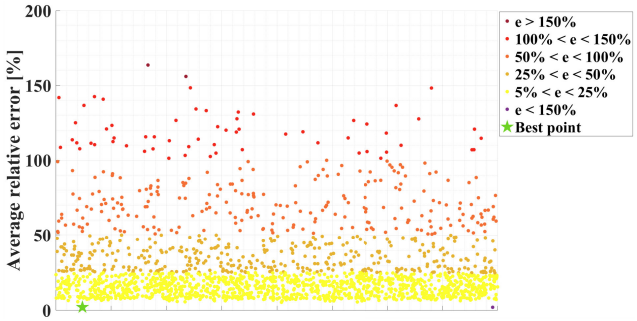

FIGURE 3. The average relative error derived from various combinations of the fitting parameters for dynamic validation.

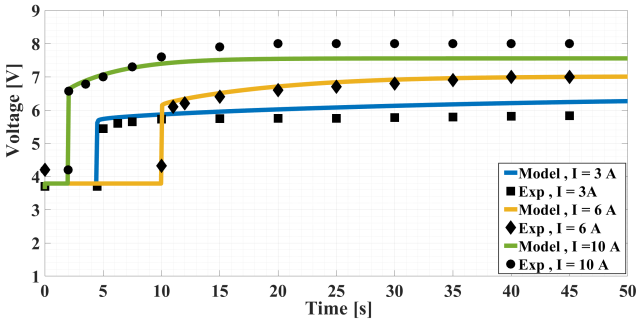

FIGURE 4. Comparison of the stack voltage between the best point obtained from the model and experiment with the applied currents of 3, 6 and 10 A.

TABLE 5. Specifications of the PEM electrolyser used for the dynamic validation [64].

Parameter	Value	Unit
A	50	cm^2
c_{p,H_2}	14337	J/kg.K
c_{p,H_2O}	4179	J/kg.K
c_{p,O_2}	920.50	J/kg.K
F	96485.33	A.s/mol
M_{H_2}	0.002	kg/mol
M_{H_2O}	0.018	kg/mol
M_{O_2}	0.032	kg/mol
n	3	-
P_{an}	1	bar
P_{ca}	10.50	bar
R_u	8.31	J/K.mol
T_{in}	20	°C
$\widehat{\Delta H^0_{H_2}}$	0	J/mol
$\widehat{\Delta H^0_{H_2O}}$	-285830	J/mol
$\widehat{\Delta H^0_{O_2}}$	0	J/mol
δ_{an-ca}	0.08	mm
δ_{mem}	0.30	mm
ϵ	0.30	-
ε_{H_2}/k	59.70	K
ε_{H_2O}/k	809.10	K
ε_{O_2}/k	106.70	K
Θ_{H_2}	2.827	Å
Θ_{H_2O}	2.641	Å
Θ_{O_2}	3.467	Å
ξ	4	-

TABLE 6. Fitted parameters for dynamic validation.

Parameter	Considered range	Fitted value	Unit
$j_{0,an-ref}$	$10^{-11} - 10^{-4}$	3.90×10^{-6}	A/cm^2
$j_{0,ca-ref}$	$10^{-6} - 10^{-1}$	2.52×10^{-2}	A/cm^2
α_{an}	0.4 – 2.5	0.49	-
α_{ca}	0.1 – 1	0.12	-

2) DYNAMIC MODE

The specifications of the electrolyser used for the dynamic validation of the developed PEM electrolyser model are shown in Table 5.

The same approach employed for the static mode was applied to the dynamic operation mode. Also, the fitting parameters were varied within the same range as described in the static mode section. The chosen set of fitting parameters as well as the explored range of the four fitting parameters are shown in Table 6.

Concerning the dynamic mode, three various cases were examined where in the reference case, a step current with an amplitude of 6 A was applied to the electrolyser. The relative errors obtained for different combinations of fitting parameters are depicted in Fig. 3, and the set yielding a 2.03 % error was selected.

Thereafter, the amplitude of the step current was changed to 3 A and 10 A, resulting in relative errors of 5.21% and 4.55%, respectively, as shown in Fig. 4. This led to an average relative error of 3.93% for the studied cases in the dynamic operation mode.

The higher relative error observed in the dynamic mode compared to the static mode is mainly due to the unspecified thermal characteristics, such as ΔT, in the experiment. In the simulations, the inlet temperature for all cases was set to 20 °C, and ΔT was set to 10. However, if these parameters were adjusted to more closely match the experimental values, the obtained error could be reduced, as the thermal parameters have a significant impact on the response of the electrolyser [42]. Additionally, the higher relative error in cases other than the reference case in the dynamic mode is attributed to the fitting parameters not being optimal for those scenarios.

III. REVERSE OSMOSIS MODEL

In this article, the dynamics of the RO system are excluded, and a static model is developed. This assumption is based on two considerations. First, RO systems typically respond to input changes within a timescale of a few seconds, which is considered relatively fast [66], [67]. Second, as mentioned in Section I, while seawater desalination requires approximately 2–3 kWh of electricity to produce 1 m^3 of purified water, nearly 5000 kWh is required to convert the same volume of water into hydrogen and oxygen through electrolysis. As such, the energy demand of the desalination process is negligible in comparison to that of the PEM electrolyser. Consequently, the dynamic behaviour of the SWRO system is not modelled, as it does not significantly influence the overall accuracy of the seawater electrolysis process.

TABLE 7. Equations used for modelling of RO system.

No.	Equation	Reference
(70)	$Q_{\mathrm{f}} = Q_{\mathrm{b}} + Q_{\mathrm{p}}$	[68]
(71)	$Q_{\mathrm{f}}C_{\mathrm{f}} = Q_{\mathrm{b}}C_{\mathrm{b}} + Q_{\mathrm{p}}C_{\mathrm{p}}$	[68]
(72)	$J_{\mathrm{w,x}} = k_{\mathrm{w}}(\Delta P_{\mathrm{x}} - \Delta\pi_{\mathrm{x}})$	[68]
(73)	$\Delta P_{\mathrm{x}} = P_{\mathrm{fb,ave}} - P_{\mathrm{p}}$	[68]
(74)	$P_{\mathrm{fb,ave}} = \frac{(P_{\mathrm{f}}+P_{\mathrm{b}})}{2}$	[68]
(75)	$\Delta\pi_{\mathrm{x}} = \pi_{\mathrm{m,x}} - \pi_{\mathrm{p}}$	[68]
(76)	$\pi = \frac{i_{\mathrm{p}}\phi C R_{\mathrm{u}} T}{M}$	[69]
(77)	$J_{\mathrm{s,x}} = k_{\mathrm{s}}(C_{\mathrm{m,x}} - C_{\mathrm{p}}) \times 10^{-6}$	[68]
(78)	$C_{\mathrm{m,x}} = \beta_{\mathrm{x}} C_{\mathrm{fb,x}}$	[68]
(79)	$\beta_{\mathrm{x}} = (e^{-J_{\mathrm{w,x}}/(k_{\mathrm{m}}\times 3.6\times 10^{6})})S_{\mathrm{r}} + (1 - S_{\mathrm{r}})$	[70]
(80)	$k_{\mathrm{m}} = \frac{Sh.D_{\mathrm{f}}}{d_{\mathrm{h}}}$	[71]
(81)	$Sh = 0.065.Re^{0.875}.Sc^{0.25}$	[71]
(82)	$Re = \frac{\rho_{\mathrm{sw}}.v_{\mathrm{c,x}}.d_{\mathrm{h}}}{\mu_{\mathrm{sw}}}$	[71]
(83)	$Sc = \frac{\mu_{\mathrm{sw}}}{\rho_{\mathrm{sw}}.D_{\mathrm{f}}}$	[71]
(84)	$v_{\mathrm{c,x}} = \frac{Q_{\mathrm{fb,x}}}{h_{\mathrm{c}}.w}$	[69]
(85)	$d_{\mathrm{h}} = \frac{h_{\mathrm{c}}.w}{(2h_{\mathrm{c}}+2w)}$	[70]
(86)	$D_{\mathrm{f}} = D_{\mathrm{f,25}}\frac{T_{\mathrm{f}}+273.15}{25+273.15}\frac{\mu_{25}}{\mu}$	[70]
(87)	$k_{\mathrm{w}} = k_{\mathrm{w,25}} * exp(k_{wt}(\frac{1}{T_f+273.15} - \frac{1}{25+273.15}))$	[70]
(88)	$k_{\mathrm{s}} = k_{\mathrm{s,25}} * exp(k_{st}(\frac{1}{T_f+273.15} - \frac{1}{25+273.15}))$	[70]
(89)	$h_{l,x} = \delta_{\mathrm{hl}} v_{\mathrm{c,x}}^2 dx$	[69]
(90)	$Q_{p,x} = J_{w,x} w dx$	[69]
(91)	$M_{s,x} = \frac{1}{3600} J_{s,x} w dx$	[69]
(92)	$Q_p = \sum_{x=1}^{num} Q_{p,x}$	[69]
(93)	$M_s = \sum_{x=1}^{num} M_{s,x}$	[69]
(94)	$C_p = \frac{J_s}{J_w \times 1000}$	[69]
(95)	$R_{\mathrm{r}} = \frac{Q_{\mathrm{p}}}{Q_{\mathrm{f}}}$	[69]
(96)	$S_{\mathrm{r}} = 1 - (\frac{C_{\mathrm{p}}}{C_{\mathrm{m}}})$	[69]

A. RO MODEL DESCRIPTION

In the osmosis process, a semi-permeable membrane separates a diluted solution from a concentrated one, allowing water to naturally flow from the diluted to the concentrated side. Conversely, reverse osmosis involves applying an external pressure that exceeds the osmotic pressure, which forces water to migrate from the concentrated side to the dilute side. In this process, non-fresh water is fed into the RO system at high pressure, where a portion of this water passes through the membrane, resulting in a low-concentration output known as permeate, whereas the remaining water, typically at a higher concentration than the feed, exits the RO unit, referred to as brine. In this study, each element of the RO system is divided into several increments, and the associated equations are solved sequentially for each increment. Hence, the brine flow from one increment ($Q_{\mathrm{b,x}}$) serves as the feed flow for the next increment ($Q_{\mathrm{fb,(x+1)}}$), whereas the permeate from each element ($Q_{\mathrm{p,x}}$) is stored to form part of the final permeate. A schematic of a single element with a differential increment is shown in Fig. 5.

Among the various approaches for modelling RO membranes, this article utilises the solution-diffusion method. According to this method, the movement of polymer chains

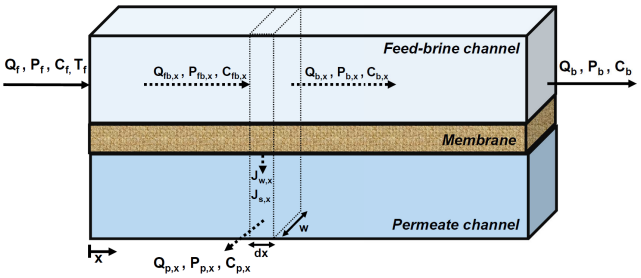

FIGURE 5. Schematic of an RO element divided into increments.

governs the permeation process, followed by diffusion through the membrane toward the permeate side [72].

The equations used for modelling the RO unit are summarised in Table 7, where all pressures are expressed in bar.

Each of the three existing sub-entities in the RO system – feed, brine, and permeate – is characterised by its flow rate (Q_{f} for feed, Q_{b} for brine, and Q_{p} for permeate), concentration (C_{f} for feed, C_{b} for brine, and C_{p} for permeate), temperature (T_{f} for feed, T_{b} for brine, and T_{p} for permeate),

and pressure (P_f for feed, P_b for brine, and P_p for permeate). In steady-state, the governing equations for flow balance and mass balance are shown in (70) and (71).

In the RO system, the water flux at increment x, indicated as $J_{w,x}$, is proportional to the driving force in the reverse osmosis process, denoted as the net driving pressure (NDP) in this study, as described in (72), where k_w is the water permeability. The NDP is the difference between ΔP_x, the applied pressure differential at increment x, and $\Delta\pi_{m,x}$, the transmembrane osmotic pressure differential at the corresponding increment. The pressure differential ΔP_x can be calculated using (73), with $P_{fb,ave}$ being the pressure in the feed-brine channel, which is calculated using (74). The transmembrane osmotic pressure differential is given by (75), where $\pi_{m,x}$ is the osmotic pressure at the membrane surface of the feed-brine channel in increment x, and $\pi_{p,x}$ represents the osmotic pressure of the permeate in increment x.

The osmotic pressure of the sub-entities can be expressed by (76), where i_p is the number of ions produced during solute dissociation, ϕ is the osmotic coefficient, and C is the concentration of the respective flow.

On the other hand, the solute flux at increment x is proportional to the difference between the solute concentration near the membrane on the feed side, $C_{m,x}$, and the permeate side of the corresponding increment, C_p, as shown in (77), where k_s is the solute permeability. The definition of $C_{m,x}$ accounts for the fact that both water and solute flux are affected by the concentration polarisation factor, β_x. This occurs because impurities are retained by the membrane. Simultaneously, there is a lateral flow, known as cross-flow, which removes these accumulated solutes from the membrane surface. The concentration polarisation factor accounts for the balance between these forces, which varies for each solute due to differing diffusion constants. Thus, the feed concentration at the membrane interface can be described using (78). The concentration polarisation factor is determined by (79), where S_r is salt rejection and k_m represents the mass transfer coefficient.

The mass transfer coefficient is defined via (80), where Sh is the dimensionless Sherwood number, D_f represents the diffusivity of the solute, and d_h stands for the hydraulic diameter of the spacer-filled channel. For a spiral wound topology, the Sherwood number is calculated using (81), where Re is the Reynolds number and Sc is the Schmidt number of the solute. The Reynolds and Schmidt numbers are determined employing (82) and (83), respectively, where ρ_{sw} is the seawater density, $v_{c,x}$ indicates the cross-flow velocity in the feed-brine channel for increment x, and μ_{sw} is the dynamic viscosity of seawater. The seawater density and viscosity data utilised in this article are provided in Table 12 and Table 13 in Appendix A and Appendix B, successively. The cross-flow velocity can be derived using (84), where h_c is the channel height and w represents the channel width. The hydraulic diameter is calculated using (85).

Diffusivity is calculated using (86), where $D_{f,25}$ represents the diffusivity of seawater at 25 °C, and μ_{25} is the viscosity of seawater at 25 °C. This equation also accounts for the temperature dependency of diffusivity.

Given the significant effect of temperature on the fluxes in the RO system, a correction factor is introduced to modify water and solute permeability, ensuring more precise calculations of water and solute fluxes. The empirical relationships expressed in (87) and (88) are used to modify the values of $k_{w,25}$ and $k_{s,25}$, respectively, at different feed water temperatures. In these equations, k_{wt} and k_{st} are temperature coefficients for water and solute transport, successively. These coefficients are derived through regression analysis of water permeability data obtained across various temperatures.

Because of head loss through the channel, the pressure in the feed-brine channel also drops. The head loss over an incremental length of the membrane, which is a function of feed velocity, can be determined using (89), where δ_{hl} is the head loss coefficient.

The permeate flow rate and the mass of solute passing through the membrane are calculated as the product of water flux and solute flux, respectively, and the area of an increment, as described in (90) and (91).

Once (70)-(91) are solved for all increments, the overall performance of the RO system can be evaluated. The total permeate production of an RO element is obtained by summing the permeate produced in each increment, as shown in (92). Likewise, the salt transfer through the membrane in one element is the sum of salt that migrates through the membrane in each increment, as expressed in (93). Based on these parameters, the permeate concentration can then be calculated using (94).

Finally, the performance of the RO system is mainly evaluated using two key factors, namely, the recovery, R_r and salt rejection, S_r, as quantified in (95) and (96), respectively.

B. RO MODEL VALIDATION

In this section, the RO model, developed using the discussed equations in the previous section and simulated in Matlab/Simulink, is validated against experimental data as well as the results obtained from WAVE commercial software (formerly known as ROSA), as reported in [73] and [74]. The [73] is selected due to the availability of both experimental and WAVE results across a broad range of operating conditions. Although WAVE is a software based on the mathematical modelling of RO systems, it is widely recognised as one of the most reliable tools in the water treatment field [73], [75]. Nevertheless, the operating points examined in [73] involve water with lower total dissolved solids (TDS) values, more comparable to brackish water than seawater, resulting in lower feed pressure compared to seawater desalination. To ensure the model is valid for higher TDS levels, such as those in seawater, the [74] is also included, as it provides experimental results of high-pressure seawater desalination.

Regarding [73], the results from the developed model in this article are compared with those from experimental

TABLE 8. Specifications of the RO unit used for the validation based on [73].

Parameter	Value	Unit
A_{mem}	37.2	m^2
C_{f}	2000-5000	ppm
$D_{\text{f},25}$	1.611×10^{-9}	m^2/s
h_{c}	0.125	mm
h_{l}	0.1	bar
i_{p}	2	-
$k_{\text{s},25}$	2×10^{-5}	m/h
k_{st}	-3281	K
$k_{\text{w},25}$	2.85	$\text{L}/(\text{m}^2.\text{h.bar})$
k_{wt}	-2849	K
l	1.02	m
num	10	-
P_{f}	7-11	bar
Q_{f}	$26 - 45$	m^3/day
T_{f}	15	°C
Φ	1	-

data and WAVE at two different feed pressures, 7 bar and 11 bar, each at feed concentrations of 2000, 3000, 4000, and 5000 ppm. The range of conditions is chosen to ensure that the model is valid under various operating scenarios. To this end, the recovery, indicating the quantity of treated water produced by the RO system, is used as one of the verification parameters. Moreover, to ensure the model precisely estimates water quality, the salt rejection of the RO model is compared with the experimental data and WAVE software results. These two factors are selected for comparison because in a coupled model of an RO system and electrolyser accurately estimating the recovery rate and salt rejection is essential, as it ensures that the electrolyser consistently receives water of the necessary quantity and quality. The employed parameters for RO validation, based on [73], are listed in Table 8.

In Fig. 6, the model is compared with experimental data and WAVE at the experimental pressure of 7 bar. Fig. 6a presents the recovery obtained from the model alongside the experimental and WAVE results, whereas Fig. 6b illustrates the comparison of salt rejection and permeate concentration between the developed model, experimental data and WAVE.

Fig. 7 shows the results derived from the model in addition to the experimental and WAVE results at the experimental pressure of 11 bar. The comparison between the recovery values obtained from the model, experiment and WAVE is depicted in Fig. 7a, and Fig. 7b shows the comparison of salt rejections as well as permeate concentrations.

In Fig. 6a and Fig. 7a, as feed concentration increases at a constant feed pressure, the recovery decreases. This occurs since, according to (72), (75), and (76), at constant feed pressure, a rise in feed concentration increases the osmotic pressure, which in turn reduces the driving force, resulting in a lower permeate flow rate and thus a lower recovery rate.

As for water quality in Fig. 6b and Fig. 7b, at a constant feed pressure, increasing the feed concentration leads to a decrease in permeate flow rate. Additionally, considering (77) and (78), the salt passage through the membrane increases.

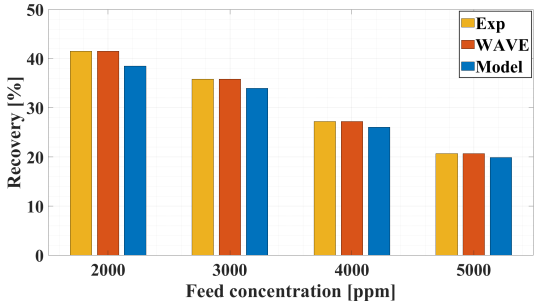

(a) Comparison of the recovery rate between the developed model, experimental data, and WAVE at 7 bar

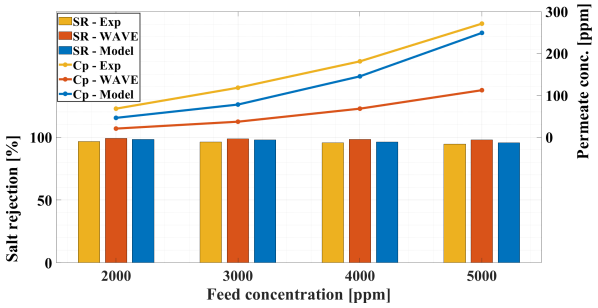

(b) Comparison of salt rejection and permeate concentration between the developed model, experimental data, and WAVE at 7 bar

FIGURE 6. Comparison of the developed model, experimental data, and WAVE at the experimental pressure of 7 bar.

Consequently, based on (94), the permeate concentration also rises, leading to a reduction in salt rejection as described in (96).

Regarding the accuracy of the model, the average relative error between the model, the experiment and WAVE is calculated using the same approach as in (69). Fig. 8 displays the average relative error for the specified feed concentrations at feed pressures of 7 bar and 11 bar, as well as the overall average relative error across all investigated cases for both feed pressures.

In Fig. 8, the average relative error for the recovery between the model and both the experiment and WAVE at feed pressures of 7 bar and 11 bar is 5.16% and 2.13%, respectively, resulting in an overall average relative error of 3.64% across all investigated cases with different feed concentrations and pressures. Besides, the average relative error for salt rejection between the model and the experiment, as well as between the model and WAVE, is 1.28% and 1.55% at 7 bar, successively. At 11 bar, the average relative error for salt rejection between the model and experiment is 1.69%, and between the model and WAVE, it is 0.32%. This yields an overall average relative error of 1.48% between the model and experiment, and 0.93% between the model and WAVE for salt rejection across all the explored cases.

The discrepancy between the model and experimental results, as well as the obtained results from WAVE, primarily arises from the fact that the developed model employs

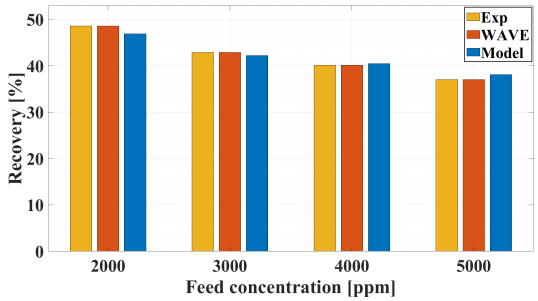

(a) Comparison of the recovery rate between the developed model, experimental data, and WAVE at 11 bar

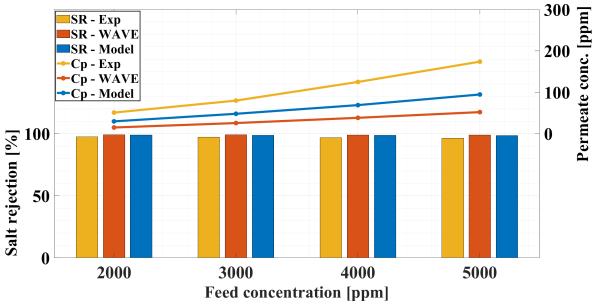

(b) Comparison of salt rejection and permeate concentration between the developed model, experimental data, and WAVE at 11 bar

FIGURE 7. Comparison of the developed model, experimental data, and WAVE at the experimental pressure of 11 bar.

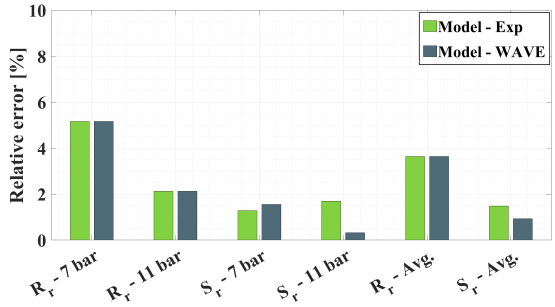

FIGURE 8. Average relative error between the developed RO model, experiment, and WAVE.

parameters for seawater, such as viscosity and density, which contains a concentration of roughly 35000 ppm. However, the low concentration of water utilised in the experiment is close to that of brackish water. Moreover, the WAVE software employs experimental equations for the associated membrane, whereas this model relies on mathematical equations to govern the RO process. Regarding the higher error observed at lower concentrations, as can be seen in Appendix A and Appendix B, it can be attributed to the fact that the accurate data for seawater is only available starting from 10000 ppm, resulting in higher error when extrapolating to lower concentrations.

To confirm the applicability of the developed model at higher TDS values, similar to those of seawater, the obtained

TABLE 9. Specifications of the RO unit used for the validation based on [74].

Parameter	Value	Unit
A_{mem}	1.14	m^2
C_{f}	25000-40000	ppm
$D_{\mathrm{f},25}$	1.611×10^{-9}	m^2/s
h_{c}	0.043	cm
h_{l}	0.1	bar
i_{p}	2	-
$k_{\mathrm{s},25}$	2×10^{-4}	m/h
k_{st}	-3281	K
$k_{\mathrm{w},25}$	2.20	L/(m^2.h.bar)
k_{wt}	-2849	K
l	0.94	m
num	10	-
P_{f}	50-80	bar
Q_{f}	$14.50 - 15.30$	m^3/day
T_{f}	20	°C
Φ	1	-

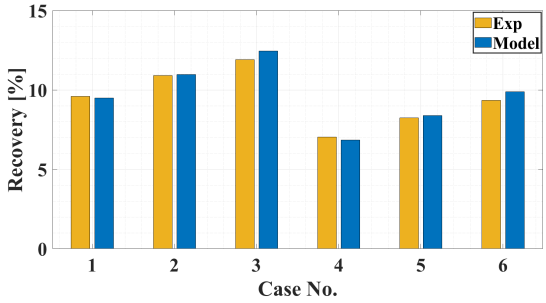

(a) Comparison of recovery rate between the developed model and experimental results

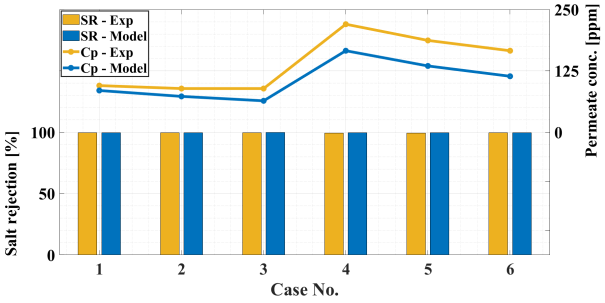

(b) Comparison of salt rejection and permeate concentration between the developed model and experimental results

FIGURE 9. Comparison between the developed model and experimental results for seawater.

results from the developed model are compared with the experimental data, detailed in [74]. The same parameters as the previous case, i.e., the recovery and salt rejection, are chosen as the comparison criteria. The utilised parameters for RO validation based on the [74] are summarised in Table 9.

Fig. 9 shows the results obtained from the model alongside experimental results for six various cases. The feed pressure is 50 bar for cases 1 and 4, 55 bar for cases 2 and 5, and 60 bar for cases 3 and 6. Additionally, the feed concentration for the first three cases is 25000 ppm, whereas for the last three cases it is 35000 ppm.

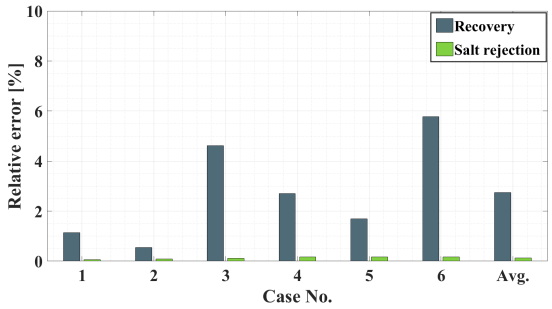

FIGURE 10. Average relative error between the developed RO model and experimental results for seawater.

Fig. 9a compares the recovery rates derived from the model and experiment, whereas Fig. 9b presents a comparison of salt rejections and permeate concentrations obtained from both the model and the experimental results.

In Fig. 9a, it is evident that, at a constant feed concentration, the recovery increases as feed pressure rises from case 1 to 3 and from case 4 to 6. This is due to the increase in the NDP, which enhances water passage through the membrane, as described by (72). Moreover, at a constant feed pressure, such as in cases 1 and 4, an increase in feed concentration raises the osmotic pressure, which reduces the NDP and, in turn, decreases the water passage through the membrane according to (72).

About the accuracy of the model, the relative error between the model and experimental results is derived using (69), as shown in Fig. 10. The average relative errors for recovery and salt rejection across all explored cases are 2.74% and 0.13%, respectively, which validates the accuracy of the developed model.

IV. SWRO-PEM ELECTROLYSER COUPLED MODEL

After ensuring that the developed models are sufficiently accurate, in this section, the PEM electrolyser and RO models are upscaled to create a more realistic scenario. Afterwards, the models are coupled, and the performance of the integrated system is assessed.

A. PEM ELECTROLYSER UPSCALING

In this article, a 2 MW PEM electrolyser is considered, which is a typical capacity for commercial PEM electrolysers for integrating with RESs [76]. For this purpose, the validated cells from Section II are used as the basis for upscaling. Also, the currently feasible ratings and sizes for PEM electrolysers reported by IRENA have been utilised to ensure the scenario is as realistic as possible [76].

It is notable that exploring RES type and power input variations to the electrolyser, which affect its sizing, is beyond the scope of this study. However, the approach presented in this article allows for modelling various sizing scenarios based on specific applications. Further details on scaling the electrolyser capacity based on RES type and power input capacity can be found in [77] and [78].

TABLE 10. Specifications of the upscaled PEM electrolyser.

Parameter	Value	Unit
A	0.1	m^2
j	0.2–2	A/cm^2
n	420	-
P_{an}	1	bar
P_{ca}	30	bar
Power	2	MW
V_{stack}	1	kV

To start with, the PEM stack voltages around 0.9-1 kV are deemed acceptable, with 1 kV assumed in this study. Given the assumed capacity of the electrolyser, this yields a rated current of 2 kA flowing in the stack. To maintain a reasonable current density of 2 A/cm^2 at rated capacity, the active area of the cell validated in Section II is enlarged to 0.1 m^2. To attain the aforementioned voltage using the enlargened cells, 420 cells need to be stacked. This results in approximately 2.4 V per cell, which is within the accepted range of 1.4-2.5 V [76]. Additionally, the partial load operation of the PEM electrolyser is taken into account. To eliminate the start-up and shut-down time for nitrogen purging, a minimum operation capacity of 10% is maintained for the electrolyser [79]. Thus the electrolyser operates between 10% and 100% load, resulting in a current density ranging from 0.2 to 2 A/cm^2, and thus a current varying from 0.2 to 2 kA. The main parameters of the PEM stack are detailed in Table 10.

B. SWRO UPSCALING

Theoretically, based on (6) and (12), to produce $nI/2F$ moles of hydrogen per second via electrolysis, $nI/2F$ moles of water per second is required. Considering the molar weights of water and hydrogen, this translates to 9 kg of water, or roughly 9 L, for the generation of 1 kg of hydrogen. Nonetheless, more water is injected into the commercial electrolyser, for example, 10 L for Siemens-Silyzer-300, 11.1 L for Hydrogenics-HyLZER and CHE hydrogen generation plant, and 15.5 L for Hydrogenics' PEM electrolyser [80].

This additional water is injected for several reasons. First, it helps with cooling the electrolyser and extracting heat. It also ensures the membrane stays hydrated, which is crucial for maintaining high conductivity. Furthermore, due to system inefficiencies, a portion of water may evaporate which needs to be accounted for. Finally, a portion of the water does not undergo electrolysis and instead migrates through the membrane, as discussed in Section II. Thus, a safety margin is typically included for this extra water. Based on the aforementioned amount of water needed for commercial electrolysers, this article applies a safety factor of 1.25 for the additional required water. Given the known number of cells in the upscaled PEM electrolyser and the operating current, using the considered safety factor, the needed amount of water can be calculated. For the rated operation of the electrolyser, around 8.5 m^3/day of pure water is needed, decreasing to approximately 4.25, 2.12,

TABLE 11. Specifications of the upscaled SWRO unit.

Parameter	Value	Unit
$C_{\mathrm{f,1st}}$	35000	ppm
$k_{\mathrm{s,25,1st}}$	2×10^{-5}	m/h
$k_{\mathrm{s,25,2nd}}$	5×10^{-5}	m/h
$k_{\mathrm{w,25,1st}}$	2.85	L/(m^2.h.bar)
$k_{\mathrm{w,25,2nd}}$	3.6	L/(m^2.h.bar)
$Q_{\mathrm{f,1st}}$	20	m^3/day
$Q_{\mathrm{p,rated}}$	8.5	m^3/day
$R_{\mathrm{r,rated,1st}}$	50	%
$R_{\mathrm{r,rated,2nd}}$	85	%
Stages	2	-
T_{f}	10	°C

and 0.85 m^3/day for 50%, 25% and 10% operation of the PEM electrolyser, as the required water changes linearly with respect to the current.

In terms of water quality, conventional PEM electrolysers are typically supplied with water having a purity of around less than 10 ppm TDS [22]. Using water with a higher TDS accelerates the ageing rate and adversely affects the performance of the electrolyser. Thus, in this article, the PEM electrolyser is fed with water having a TDS of less than 5 ppm to provide an extra level of precaution.

In RO systems, the brine from one stage can be fed into a subsequent stage to enhance the recovery rate, a process known as a multistage or brine-staged system. Alternatively, the permeate from one stage can be passed to a second stage to improve solute removal, referred to as a two-pass or permeate-staged system. Since the water source in this study is seawater with a high TDS of around 35000 ppm, reaching a TDS of less than 5 ppm is challenging. Nevertheless, it has been demonstrated that passing the permeate from the first stage of SWRO through a second stage can reduce the TDS to below 5 ppm [22]. Hence, this article considers a two-pass SWRO system to achieve a TDS of less than 5 ppm.

As for the recovery, the parameters are adjusted to achieve a recovery of 50% for the first pass and 85% for the second pass under rated conditions, which are standard values for high-pressure and low-pressure RO systems, respectively [69].

The main characteristics of the SWRO unit are presented in Table 11.

C. COUPLING THE UPSCALED SYSTEMS

There are two procedures for controlling the permeate flow rate in an RO system, i.e. changing the feed flow rate, and altering the feed pressure. However, the feed pressure is the primary variable that governs the permeate flow rate, as the driving force of the process can be directly regulated by adjusting the feed pressure, whereas changes in the feed flow rate have a less direct impact on the feed flow rate, as shown in Fig. 11. Consequently, in this study, the permeate flow rate is controlled by adjusting the feed pressure. It is also worth noting that Fig. 11 is generated based on the RO element described in Section III at the feed concentration of 5000 ppm.

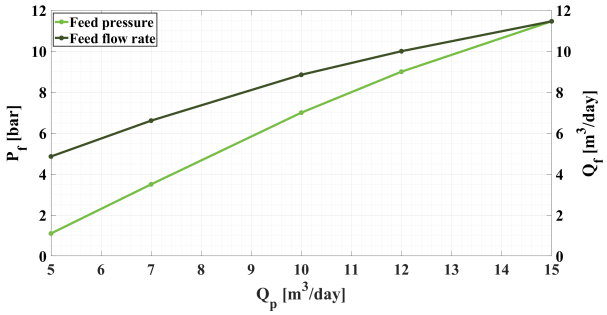

FIGURE 11. Variation of permeate flow rate as a function of feed pressure and feed flow rate.

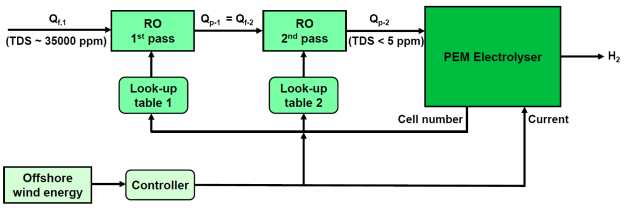

FIGURE 12. Control scheme of the SWRO-PEM electrolyser model.

Additionally, the P_{f}–Q_{p} curve in Fig. 11 exhibits an almost linear relationship between the permeate flow rate and the feed pressure, as also verified in [81] for various feed concentrations. This linearity offers the advantage of using a lookup table to control the RO system when coupled with the electrolyser during single-system simulations. Given that the integrated model is primarily designed for large-scale simulations, which include multiple complex power system elements, such as generators and transformers, this approach significantly enhances computational efficiency. In this method, the feed pressure of each RO pass is regulated through a control signal that dynamically responds to variations in the electrolyser current to meet its water demand.

To establish this control strategy, prior to coupling the PEM electrolyser and SWRO models, the operation of both the first and second passes was examined across a range from 10% to 100% capacity, with a resolution of 5%, to be consistent with the upscaled PEM electrolyser. The control scheme of the SWRO unit and an overview of the integrated SWRO-PEM model are shown in Fig. 12 and Fig. 13, respectively.

In summary, the operation of the two-pass SWRO system is first evaluated across its operating range, from 10% to full capacity. The integrated SWRO–PEM system is then implemented, as depicted in Fig. 12. Due to the fluctuating nature of offshore wind energy, the power output from the offshore wind turbines block, shown in Fig. 12, varies accordingly, which in turn affects the output of the current controller in the following block of the same figure. This current, combined with the number of cells in the electrolyser stack, determines the required water flow from the SWRO system, as described by (6). The current values

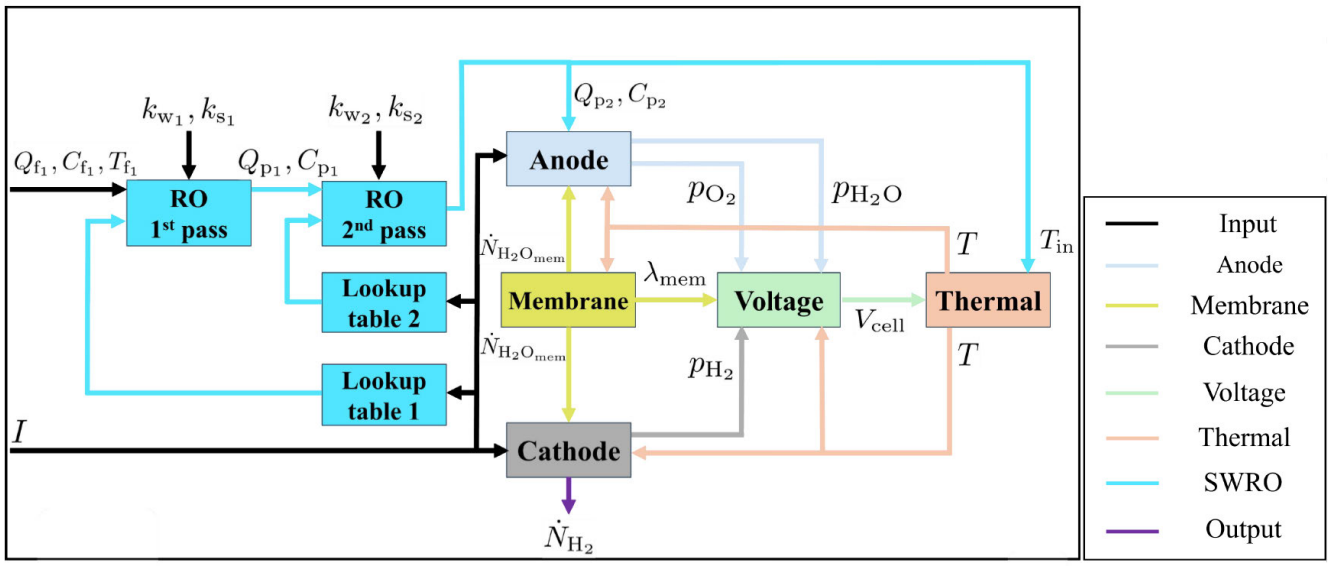

FIGURE 13. An overview of the coupled SWRO-PEM electrolyser model.

are subsequently mapped, using lookup tables 1 and 2, to the feed pressures of the first and second RO passes, respectively. As shown in Fig. 11, this approach effectively regulates the permeate flow rates of both passes.

It should be noted that this article does not consider the current controller presented in Fig. 12; instead, the current waveform is directly generated and applied to the electrolyser. A controller scheme for translating power to current based on grid frequency variations for providing frequency ancillary services has been proposed in [79].

D. RESULTS

The step response of the electrolyser, starting from no load and then shifting to full load, 50% of full load, 25% of full load, 10% of full load, and subsequently ramping back up to 25%, 50%, and 100% of full load, is shown in Fig. 14. Fig. 14a shows the applied step current waveform, whereas Fig. 14b and Fig. 14c depict the voltage on the 2 MW PEM stack, and the power consumed by the electrolyser, respectively.

It is important to note that the response time of the electrolyser is slower at lower current densities. This can be explained by the fact that, at lower current densities, activation overvoltage is the dominant term in the total stack voltage, whereas, at higher current densities, ohmic overvoltage becomes the main contributor to the stack voltage. Since activation overvoltage follows an exponential curve, at lower loads, changes in the current cause the stack voltage to behave more like the activation overvoltage pattern, leading to a more gradual response. On the other hand, at higher loads, when current density changes, the response is faster because ohmic overvoltage, which is directly proportional to the current, has a more immediate impact on the stack voltage.

The behaviour of the upscaled SWRO system suitable for the 2 MW PEM electrolyser is presented in Fig 15. Fig. 15a shows the recovery ratios of the first and second passes of the SWRO system, whereas Fig. 15b and Fig. 15c depict the salt rejection and permeate concentration of the two passes. This figure corresponds to the changes depicted in Fig. 14.

It is worth mentioning that, although the first pass is able to produce fresh water with a TDS of around 150 ppm at its highest, this level is still insufficient for the PEM electrolyser, which requires a TDS of less than 5 ppm. Regardless, as shown in Fig. 15c, the permeate concentration after the second pass is below 5 ppm even at its worst.

As mentioned earlier, adjusting the feed pressure regulates the NDP, and hence the required amount of water. When the feed pressure is decreased at a constant feed flow rate, the permeate flow rate is reduced, leading to a lower recovery ratio at lower loads, as shown in Fig. 15. Additionally, considering Fig. 15b, increasing feed pressure reduces salt rejection, yielding a higher permeate concentration in both passes. This occurs because, when the feed pressure is decreased, the permeate from each pass becomes more saline, leading to an increased level TDS level.

Furthermore, it can be seen that the first pass exhibits a lower recovery ratio but higher salt rejection compared to the second pass. This is expected since the membrane utilised in the first pass typically has smaller pores, resulting in a higher salt rejection and reduced water passage, thereby a lower recovery rate. The choice of the membrane with smaller pores is because the first feed is more saline. As shown in Fig. 15c, the first pass reduces the feed concentration from 35000 ppm to a permeate concentration of around 150 ppm at its worst. In contrast, the second pass commonly handles feed water with a lower concentration, similar to brackish water. Therefore, to increase the recovery rate, the pores of the

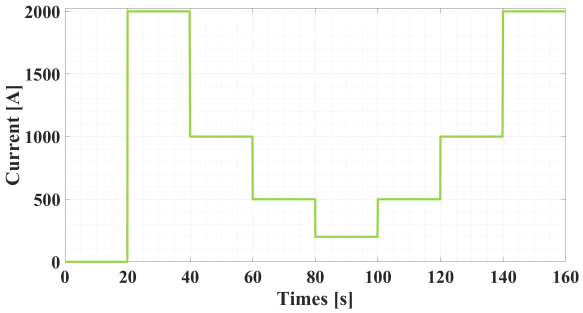

(a) Applied step current waveform

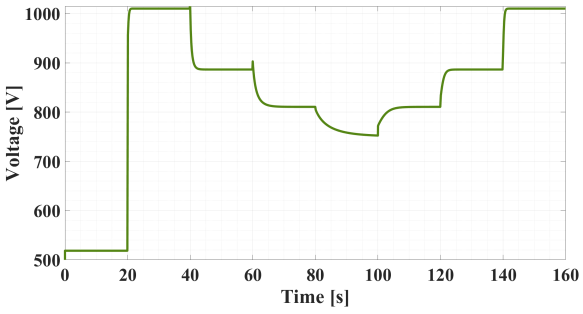

(b) Dynamic voltage waveform

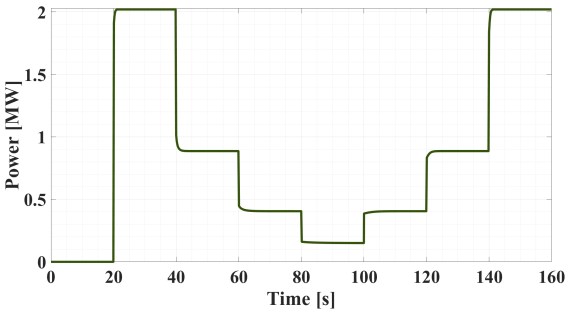

(c) Dynamic power waveform

FIGURE 14. Dynamic step response of the 2 MW PEM electrolyser.

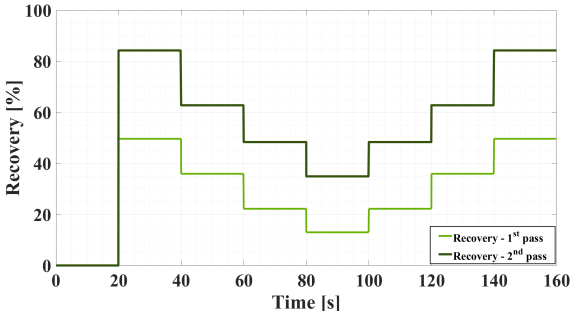

(a) Recovery rate of the first and second passes

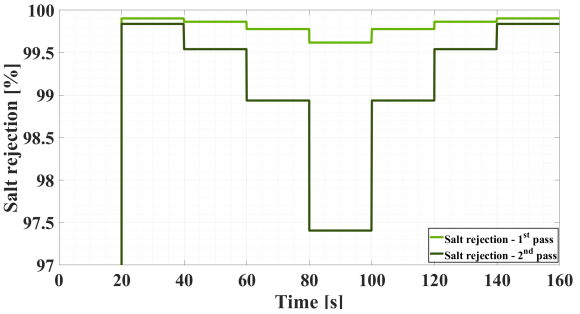

(b) Salt rejection of the first and second passes

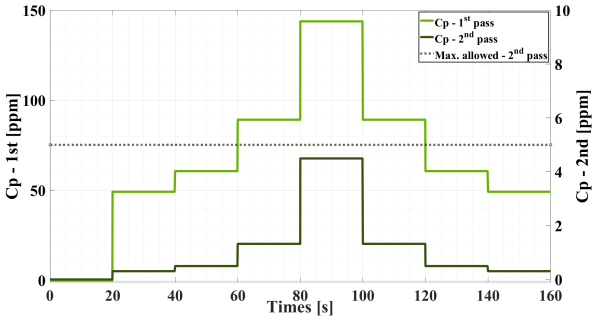

(c) Permeate concentration of the first and second passes

FIGURE 15. Behaviour of the two-pass SWRO system.

membrane are larger. In the modelling stage, this membrane behaviour is simulated by combining a lower value of k_s (indicating higher salt rejection) with a lower value of k_w for the first pass compared to the second one, and vice versa for the second pass, as shown in Table 11. It is important to note that the lower recovery in the first pass, compared to the second, can also be explained by the high salt concentration of seawater, which increases the osmotic pressure.

To verify the accuracy of the control method in estimating the required amount of water, the theoretical water demand of the electrolyser is compared with the actual amount provided by the control method, as depicted in Fig. 16. Fig. 16a shows the comparison of the actual water demand, derived using (6) with a safety factor of 1.25, and the estimated amount of water, whereas Fig. 16b illustrates the discrepancy between these two values, yielding an average relative error of 1.20% over the evaluated timeframe. The results indicate that the control method can effectively estimate the actual water required.

V. CONCLUSION

In this article, a coupled model of an SWRO system and a PEM electrolyser was developed in Matlab/Simulink, which facilitates further studies in offshore hydrogen production. Moreover, the model can be integrated into large-scale power system simulations without introducing excessive complexity.

By following the steps described in this article, the offshore hydrogen production system can be examined under different operating conditions upon sizing the electrolyser based on factors such as available input power, available offshore area, and hydrogen demand. This integrated model is essential for advancing offshore hydrogen, offering important insights into green hydrogen production using seawater as the feedwater.

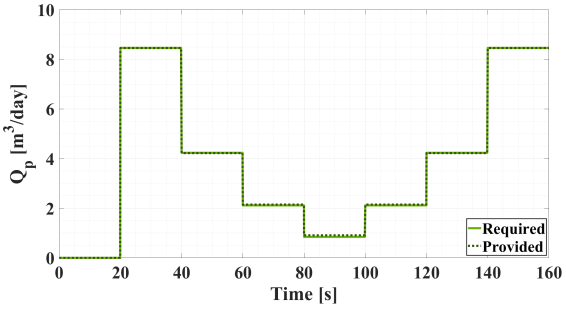

(a) Water demand of the PEM electrolyser and amount provided by the SWRO unit

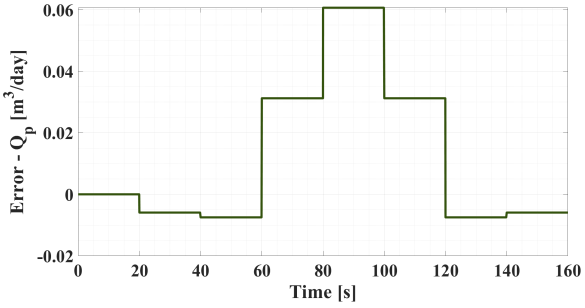

(b) Discrepancy between the water demand of the PEM electrolyser and the amount provided by the SWRO unit

FIGURE 16. Comparison between the required water for the PEM electrolyser and the amount provided by the SWRO system.

In this study, the PEM electrolyser incorporates five modules: anode, cathode, membrane, voltage and thermal, where the relevant equations are compiled. Also, the model was validated against the experimental data, showing an average relative error of 0.66% and 3.93% in static and dynamic operation modes, respectively.

Using the solution-diffusion method, a model for the SWRO system was developed. Thereafter, validation against the experimental data at low TDS values exhibited an average relative error of 3.64% for recovery and 1.48% for salt rejection. When compared with WAVE software, the model demonstrated an average relative error of 3.64% for recovery and 0.96% for salt rejection. At seawater TDS levels, the model showed an average relative error of 2.74% and 0.13% for recovery and salt rejection, respectively, compared to experimental results.

Following validation, the PEM electrolyser and SWRO models were upscaled to simulate a realistic scenario: a 2 MW electrolyser containing 420 cells coupled with a two-pass SWRO system, with rated recovery rates of 50% and 85% for the first and second pass, respectively, and a production capacity of 8.5 m^3/day. To efficiently couple the validated models and enhance computational efficiency, an uncomplicated control method based on lookup tables, generated before coupling the models, was proposed, taking advantage of the nearly linear relationship between feed pressure and permeate flow rate. The water injected into the electrolyser was delivered at a maximum of 4.5 ppm TDS, and the control method estimates the required water quantity with a 1.20% error.

Notably, the integrated model allows for adjustments to various parameters, such as feed flow rate, feed concentration, feed temperature, etc, as well as electrolyser parameters like inlet temperature, current density, etc.

Nevertheless, the coupled model can further be improved by incorporating more physics-based equations instead of empirical ones, such as those for electro-osmotic drag in the PEM electrolyser or the mass transfer coefficient in the SWRO model. Although empirical equations simplify the modelling process and enhance computational efficiency, they are generally formulated based on specific datasets obtained under specific operating conditions, such as temperature, pressure, and current density. Consequently, their reliability may decrease when applied outside these original conditions. Therefore, the use of empirical correlations represents a major limitation of the model for both the SWRO and PEM electrolyser systems. Furthermore, other BoP components could be integrated into the model, allowing for the evaluation of their impact on hydrogen production. This may include detailed modelling of offshore wind turbines or other RESs based on the application, depending on the application, along with their associated power conditioning units and converters. Finally, future studies could also consider social, environmental and legal aspects of the coupled SWRO-PEM electrolyser.

APPENDIX A
SEAWATER DENSITY

The empirical equation employed for seawater current density is as follows [68]:

$$\rho_{sw} = 10^3(A_1F_1 + A_2F_2 + A_3F_3 + A_4F_4), \tag{97}$$

where

$$B = \frac{0.002C - 150}{150}, \tag{98}$$

$$G_1 = 0.5, \tag{99}$$

$$G_2 = B, \tag{100}$$

$$G_3 = 2B^2 - 1, \tag{101}$$

$$A_1 = 4.032219\, G_1 + 0.115313\, G_2 + 3.26 \times 10^{-4}\, G_3, \tag{102}$$

$$A_2 = -0.108199\, G_1 + 1.571 \times 10^{-3}\, G_2 - 4.23 \times 10^{-4}\, G_3, \tag{103}$$

$$A_3 = -0.012247\, G_1 + 1.74 \times 10^{-3}\, G_2 - 9 \times 10^{-6}\, G_3, \tag{104}$$

$$A_4 = 6.29 \times 10^{-4}\, G_1 - 8.7 \times 10^{-5}\, G_2 - 5.3 \times 10^{-5}\, G_3, \tag{105}$$

$$A = \frac{2T - 200}{160}, \tag{106}$$

$$F_1 = 0.5, \tag{107}$$

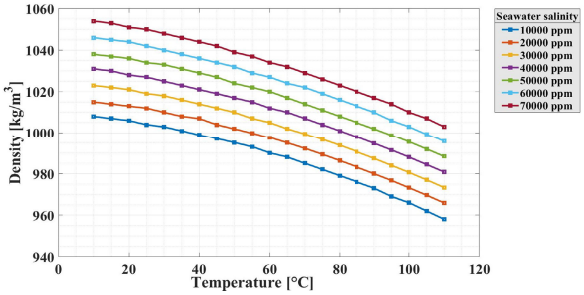

FIGURE 17. Variations in the seawater density as a function of temperature and concentration.

TABLE 12. Variations in the seawater density [kg/m^3] as a function of temperature [°C] and TDS [ppm].

T [°C]	10000	20000	30000	40000	50000	60000	70000
10	1008	1015	1023	1031	1038	1046	1054
15	1007	1014	1022	1030	1037	1045	1053
20	1006	1013	1021	1028	1036	1044	1051
25	1004	1012	1019	1027	1034	1042	1050
30	1003	1010	1018	1025	1033	1040	1048
35	1001	1008	1016	1023	1031	1038	1046
40	999	1007	1014	1021	1029	1036	1044
45	997	1004	1012	1019	1027	1034	1042
50	995	1002	1010	1017	1024	1032	1039
55	993	999.9	1007	1015	1022	1029	1037
60	990	997.5	1005	1012	1020	1027	1034
65	988	994.9	1002	1010	1017	1024	1032
70	985	992.2	999.5	1007	1014	1022	1029
75	982	989.3	996.6	1004	1011	1019	1026
80	979	986.3	993.7	1001	1008	1016	1023
85	976	983.2	990.6	997.9	1005	1013	1020
90	973	980	987.4	994.7	1002	1010	1017
95	969	976.7	984.1	991.4	998.8	1006	1014
100	966	973.2	980.6	988	995.4	1003	1010
105	962	969.6	977	984.4	991.9	999.3	1007
110	958	965.9	973.3	980.8	988.3	995.7	1003

$$F_2 = A, \tag{108}$$

$$F_3 = 2A^2 - 1, \tag{109}$$

$$F_4 = 4A^3 - 3A. \tag{110}$$

In the above equations, T is represented in °C. Utilising the above equations, the variations in the seawater density as a function of feed temperature and concentration can be shown in Fig. 17 and Table 12.

APPENDIX B
SEAWATER VISCOSITY

As for the seawater dynamic viscosity, the empirical equation suggested in [68] is used, given as:

$$\mu_{sw} = \mu_w.\mu_r.10^{-3}, \tag{111}$$

where

$$ln(\mu_{sw}) = -3.79418 + \frac{604.129}{139.18 + T}, \tag{112}$$

$$\mu_r = 1 + (V_1 \frac{C}{1000}) + V_2 \frac{C}{1000}), \tag{113}$$

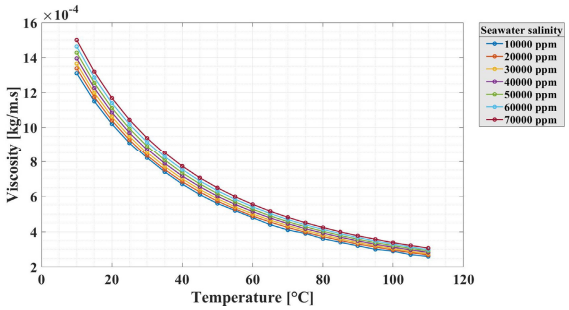

FIGURE 18. Variations in seawater viscosity as a function of temperature and concentration.

TABLE 13. Variation in seawater viscosity [kg/m.s] as a function of temperature [°C] and TDS [ppm].

T [°C]	10000	20000	30000	40000	50000	60000	70000
10	1.31	1.338	1.365	1.395	1.428	1.463	1.5
15	1.15	1.175	1.199	1.226	1.255	1.286	1.319
20	1.02	1.04	1.062	1.086	1.112	1.14	1.169
25	0.91	0.928	0.948	0.969	0.993	1.018	1.044
30	0.82	0.833	0.851	0.871	0.892	0.915	0.939
35	0.74	0.753	0.77	0.788	0.807	0.827	0.849
40	0.67	0.684	0.7	0.716	0.734	0.753	0.772
45	0.61	0.625	0.639	0.655	0.671	0.688	0.706
50	0.56	0.573	0.587	0.601	0.616	0.632	0.649
55	0.52	0.529	0.541	0.555	0.569	0.584	0.599
60	0.48	0.489	0.501	0.514	0.527	0.541	0.555
65	0.44	0.455	0.466	0.478	0.49	0.503	0.516
70	0.41	0.424	0.435	0.446	0.457	0.469	0.482
75	0.39	0.397	0.407	0.417	0.428	0.439	0.451
80	0.36	0.372	0.382	0.392	0.402	0.413	0.424
85	0.34	0.35	0.359	0.369	0.379	0.389	0.399
90	0.32	0.33	0.339	0.348	0.357	0.367	0.377
95	0.3	0.313	0.321	0.329	0.338	0.347	0.357
100	0.29	0.296	0.304	0.312	0.321	0.33	0.338
105	0.27	0.282	0.289	0.297	0.305	0.313	0.322
110	0.26	0.268	0.275	0.283	0.291	0.298	0.307

$$V_1 = 1.474 \times 10^{-3} + 1.5 \times 10^{-5}T - 3.927 \times 10^{-8}T^2, \tag{114}$$

$$V_2 = 1.0734 \times 10^{-5} - 8.5 \times 10^{-8}T + 2.23 \times 10^{-10}T^2. \tag{115}$$

It should be noted that in these equations, T is expressed in °C. By applying the above equations, the variations in seawater dynamic viscosity as a function of feed temperature and concentration are illustrated in Fig. 18 and Table 13.

ACKNOWLEDGMENT

During the preparation of this work, the authors used ChatGPT only to improve the readability and language of the manuscript, not for any scientific purposes. After using this tool, they reviewed and edited the content as needed and take full responsibility for the content of the published article.

REFERENCES

[1] S. Asiaban, N. Kayedpour, A. E. Samani, D. Bozalakov, J. D. M. De Kooning, G. Crevecoeur, and L. Vandevelde, "Wind and solar intermittency and the associated integration challenges: A comprehensive review including the status in the Belgian power system," *Energies*, vol. 14, no. 9, p. 2630, May 2021.

[2] I. Sorrenti, T. B. H. Rasmussen, S. You, and Q. Wu, "The role of power-to-X in hybrid renewable energy systems: A comprehensive review," *Renew. Sustain. Energy Rev.*, vol. 165, Sep. 2022, Art. no. 112380.

[3] X. Mao, Y. Tian, A. Yang, and G. Zhang, "Identification of equivalent circuit parameters for proton exchange membrane (PEM) electrolyzer engineering models," *IEEE Access*, vol. 12, pp. 15509–15524, 2024.

[4] N. Kopacak, H. C. Güldorum, and O. Erdinc, "Implementation of a decision-making approach for a hydrogen-based multi-energy system considering EVs and FCEVs availability," *IEEE Access*, vol. 12, pp. 114705–114721, 2024.

[5] E. Crespi, G. Guandalini, L. Mastropasqua, S. Campanari, and J. Brouwer, "Experimental and theoretical evaluation of a 60 kW PEM electrolysis system for flexible dynamic operation," *Energy Convers. Manage.*, vol. 277, Feb. 2023, Art. no. 116622.

[6] R. Mas, A. Berastain, A. Antoniou, L. Angeles, S. Valencia, and C. Celis, "Genetic algorithms-based size optimization of directly and indirectly coupled photovoltaic-electrolyzer systems," *Energy Convers. Manage.*, vol. 270, Oct. 2022, Art. no. 116213.

[7] K. Sayed, M. Khamies, A. G. Abokhalil, M. Aref, M. A. Mossa, M. Metab Almalki, and T. A. H. Alghamdi, "Feasibility study and economic analysis of PV/wind-powered hydrogen production plant," *IEEE Access*, vol. 12, pp. 76304–76318, 2024.

[8] Y. Zhang, Y. Zhang, Z. Li, E. Yu, H. Ye, Z. Li, X. Guo, D. Zhou, C. Wang, Q. Sha, and Y. Kuang, "A review of hydrogen production via seawater electrolysis: Current status and challenges," *Catalysts*, vol. 14, no. 10, p. 691, Oct. 2024.

[9] S. Jiang, H. Suo, T. Zhang, C. Liao, Y. Wang, Q. Zhao, and W. Lai, "Recent advances in seawater electrolysis," *Catalysts*, vol. 12, no. 2, p. 123, Jan. 2022.

[10] J. Mohammed-Ibrahim and H. Moussab, "Recent advances on hydrogen production through seawater electrolysis," *Mater. Sci. Energy Technol.*, vol. 3, pp. 780–807, Jan. 2020.

[11] J. Li, G. Wang, Z. Li, S. Yang, W. T. Chong, and X. Xiang, "A review on development of offshore wind energy conversion system," *Int. J. Energy Res.*, vol. 44, no. 12, pp. 9283–9297, Oct. 2020.

[12] T. Egeland-Eriksen and S. Sartori, "Techno-economic analysis of the effect of a novel price-based control system on the hydrogen production for an offshore 1.5 GW wind-hydrogen system," *Energy Rep.*, vol. 11, pp. 2633–2655, Jun. 2024.

[13] D. Jang, K. Kim, K.-H. Kim, and S. Kang, "Techno-economic analysis and Monte Carlo simulation for green hydrogen production using offshore wind power plant," *Energy Convers. Manage.*, vol. 263, Jul. 2022, Art. no. 115695.

[14] *Denmark's Energy Islands*. Accessed: Aug. 8, 2025. [Online]. Available: https://ens.dk/en/our-responsibilities/offshore-wind-power/denmarks-energy-islands

[15] T. R. Lucas, A. F. Ferreira, R. B. S. Pereira, and M. Alves, "Hydrogen production from the WindFloat Atlantic offshore wind farm: A techno-economic analysis," *Appl. Energy*, vol. 310, Mar. 2022, Art. no. 118481.

[16] M. Rezaei, A. Akimov, and E. M. A. Gray, "Techno-economics of offshore wind-based dynamic hydrogen production," *Appl. Energy*, vol. 374, Nov. 2024, Art. no. 124030.

[17] H. Becker, J. Murawski, D. V. Shinde, I. E. L. Stephens, G. Hinds, and G. Smith, "Impact of impurities on water electrolysis: A review," *Sustain. Energy Fuels*, vol. 7, no. 7, pp. 1565–1603, 2023.

[18] Z. Liu, B. Han, Z. Lu, W. Guan, Y. Li, C. Song, L. Chen, and S. C. Singhal, "Efficiency and stability of hydrogen production from seawater using solid oxide electrolysis cells," *Appl. Energy*, vol. 300, Oct. 2021, Art. no. 117439.

[19] M. A. Khan, T. Al-Attas, S. Roy, M. M. Rahman, N. Ghaffour, V. Thangadurai, S. Larter, J. Hu, P. M. Ajayan, and M. G. Kibria, "Seawater electrolysis for hydrogen production: A solution looking for a problem?" *Energy Environ. Sci.*, vol. 14, no. 9, pp. 4831–4839, 2021.

[20] B. Peñate and L. García-Rodríguez, "Current trends and future prospects in the design of seawater reverse osmosis desalination technology," *Desalination*, vol. 284, pp. 1–8, Jan. 2012.

[21] J. Kim, K. Park, D. R. Yang, and S. Hong, "A comprehensive review of energy consumption of seawater reverse osmosis desalination plants," *Appl. Energy*, vol. 254, Nov. 2019, Art. no. 113652.

[22] J. N. Hausmann, R. Schlögl, P. W. Menezes, and M. Driess, "Is direct seawater splitting economically meaningful?" *Energy Environ. Sci.*, vol. 14, no. 7, pp. 3679–3685, 2021.

[23] A. Altaee, G. Zaragoza, and H. R. van Tonningen, "Comparison between forward osmosis-reverse osmosis and reverse osmosis processes for seawater desalination," *Desalination*, vol. 336, pp. 50–57, Mar. 2014.

[24] M. Lamagna, A. M. Ferrario, D. A. Garcia, S. Mcphail, and G. Comodi, "Reversible solid oxide cell coupled to an offshore wind turbine as a poly-generation energy system for auxiliary backup generation and hydrogen production," *Energy Rep.*, vol. 8, pp. 14259–14273, Nov. 2022.

[25] D. Patel, A. Mudgal, V. Patel, and J. Patel, "Water desalination and wastewater reuse using integrated reverse osmosis and forward osmosis system," *IOP Conf. Ser., Mater. Sci. Eng.*, vol. 1146, no. 1, May 2021, Art. no. 012029.

[26] R. D'Amore-Domenech, Ó. Santiago, and T. J. Leo, "Multicriteria analysis of seawater electrolysis technologies for green hydrogen production at sea," *Renew. Sustain. Energy Rev.*, vol. 133, Nov. 2020, Art. no. 110166.

[27] B. A. Franco, P. Baptista, R. C. Neto, and S. Ganilha, "Assessment of offloading pathways for wind-powered offshore hydrogen production: Energy and economic analysis," *Appl. Energy*, vol. 286, Mar. 2021, Art. no. 116553.

[28] O. S. Ibrahim, A. Singlitico, R. Proskovics, S. McDonagh, C. Desmond, and J. D. Murphy, "Dedicated large-scale floating offshore wind to hydrogen: Assessing design variables in proposed typologies," *Renew. Sustain. Energy Rev.*, vol. 160, May 2022, Art. no. 112310.

[29] A. Singlitico, J. Østergaard, and S. Chatzivasileiadis, "Onshore, offshore or in-turbine electrolysis? techno-economic overview of alternative integration designs for green hydrogen production into offshore wind power hubs," *Renew. Sustain. Energy Transition*, vol. 1, Aug. 2021, Art. no. 100005.

[30] Z. Luo, X. Wang, H. Wen, and A. Pei, "Hydrogen production from offshore wind power in South China," *Int. J. Hydrogen Energy*, vol. 47, no. 58, pp. 24558–24568, Jul. 2022.

[31] H. T. Do Thi, T. Pasztor, D. Fozer, F. Manenti, and A. J. Toth, "Comparison of desalination technologies using renewable energy sources with life cycle, PESTLE, and multi-criteria decision analyses," *Water*, vol. 13, no. 21, p. 3023, Oct. 2021.

[32] (2024). *Desalination in the Context of Global Water Security*. [Online]. Available: https://thirdworldcentre.org/2024/03/

[33] Á. Hernández-Gómez, D. Langarica-Cordoba, P. R. Martinez-Rodriguez, H. González-Aguilar, D. Guilbert, and B. Saldivar, "Design and implementation of the Luenberger observer for estimating the voltage response of a PEM electrolyzer during supply current variations," *IEEE Access*, vol. 12, pp. 68266–68277, 2024.

[34] T. Lickert, M. L. Kiermaier, K. Bromberger, J. Ghinaiya, S. Metz, A. Fallisch, and T. Smolinka, "On the influence of the anodic porous transport layer on PEM electrolysis performance at high current densities," *Int. J. Hydrogen Energy*, vol. 45, no. 11, pp. 6047–6058, Feb. 2020.

[35] Z. Abdin, C. J. Webb, and E. M. Gray, "Modelling and simulation of a proton exchange membrane (PEM) electrolyser cell," *Int. J. Hydrogen Energy*, vol. 40, no. 39, pp. 13243–13257, Oct. 2015.

[36] K. Jing and C. Liu, "Online observer of the voltage components of the PEM electrolyzer based on the time-varying linearization of the semi-empirical model," *Energy Rep.*, vol. 9, pp. 299–307, Sep. 2023.

[37] R. Jakobsen, C. Huang, T. W. Rasmussen, and S. You, "Large-scale electrolyzer plant integration to the electrical grid: Preliminary investigation of VSC-based solutions," *Energy Rep.*, vol. 9, pp. 478–483, Oct. 2023.

[38] M. B. Hossain, M. R. Islam, K. M. Muttaqi, D. Sutanto, and A. P. Agalgaonkar, "Dynamic electrical equivalent circuit modeling of the grid-scale proton exchange membrane electrolyzer for ancillary services," in *Proc. IEEE Ind. Appl. Soc. Annu. Meeting (IAS)*, Oct. 2022, pp. 1–7.

[39] M. Nasser and H. Hassan, "Techno-enviro-economic analysis of hydrogen production via low and high temperature electrolyzers powered by PV/wind turbines/waste heat," *Energy Convers. Manage.*, vol. 278, Feb. 2023, Art. no. 116693.

[40] Á. Serna and F. Tadeo, "Offshore hydrogen production from wave energy," *Int. J. Hydrogen Energy*, vol. 39, no. 3, pp. 1549–1557, Jan. 2014.

[41] P. Ellersdorfer, A. Omar, R. A. Taylor, R. Daiyan, and G. Leslie, "Multi-effect distillation: A sustainable option to large-scale green hydrogen production using solar energy," *Int. J. Hydrogen Energy*, vol. 48, no. 81, pp. 31491–31505, Sep. 2023.

[42] S. Asiaban, D. Bozalakov, and L. Vandevelde, "Development of a dynamic mathematical model of PEM electrolyser for integration into large-scale power systems," *Energy Convers. Manage., X*, vol. 23, Jul. 2024, Art. no. 100610.

[43] T. Yigit and O. F. Selamet, "Mathematical modeling and dynamic simulink simulation of high-pressure PEM electrolyzer system," *Int. J. Hydrogen Energy*, vol. 41, no. 32, pp. 13901–13914, Aug. 2016.
[44] F. Z. Aouali, M. Becherif, H. S. Ramadan, M. Emziane, A. Khellaf, and K. Mohammedi, "Analytical modelling and experimental validation of proton exchange membrane electrolyser for hydrogen production," *Int. J. Hydrogen Energy*, vol. 42, no. 2, pp. 1366–1374, Jan. 2017.
[45] H. Gorgun, "Dynamic modelling of a proton exchange membrane (PEM) electrolyzer," *Int. J. Hydrogen Energy*, vol. 31, no. 1, pp. 29–38, Jan. 2006.
[46] X. Li, S. Qu, H. Yu, M. Hou, Z. Shao, and B. Yi, "Membrane water-flow rate in electrolyzer cells with a solid polymer electrolyte (SPE)," *J. Power Sources*, vol. 190, no. 2, pp. 534–537, May 2009.
[47] Á. Hernández-Gómez, V. Ramirez, and D. Guilbert, "Investigation of PEM electrolyzer modeling: Electrical domain, efficiency, and specific energy consumption," *Int. J. Hydrogen Energy*, vol. 45, no. 29, pp. 14625–14639, May 2020.
[48] A. Z. Weber, R. L. Borup, R. M. Darling, P. K. Das, T. J. Dursch, W. Gu, D. J. Harvey, A. Kusoglu, S. Litster, M. M. Mench, R. Mukundan, J. P. Owejan, J. G. Pharoah, M. Secanell, and I. V. Zenyuk, "A critical review of modeling transport phenomena in polymer-electrolyte fuel cells," *J. Electrochemical Soc.*, vol. 161, no. 12, pp. F1254–F1299, 2014.
[49] H. Kim, M. Park, and K. S. Lee, "One-dimensional dynamic modeling of a high-pressure water electrolysis system for hydrogen production," *Int. J. Hydrogen Energy*, vol. 38, no. 6, pp. 2596–2609, Feb. 2013.
[50] E. Hernández-Pacheco, D. Singh, P. N. Hutton, N. Patel, and M. D. Mann, "A macro-level model for determining the performance characteristics of solid oxide fuel cells," *J. Power Sources*, vol. 138, nos. 1–2, pp. 174–186, Nov. 2004.
[51] A. Awasthi, K. Scott, and S. Basu, "Dynamic modeling and simulation of a proton exchange membrane electrolyzer for hydrogen production," *Int. J. Hydrogen Energy*, vol. 36, no. 22, pp. 14779–14786, Nov. 2011.
[52] D. S. Falcão and A. M. F. R. Pinto, "A review on PEM electrolyzer modelling: Guidelines for beginners," *J. Cleaner Prod.*, vol. 261, Jul. 2020, Art. no. 121184.
[53] R. García-Valverde, N. Espinosa, and A. Urbina, "Simple PEM water electrolyser model and experimental validation," *Int. J. Hydrogen Energy*, vol. 37, no. 2, pp. 1927–1938, Jan. 2012.
[54] L. Järvinen, P. Puranen, A. Kosonen, V. Ruuskanen, J. Ahola, P. Kauranen, and M. Hehemann, "Automized parametrization of PEM and alkaline water electrolyzer polarisation curves," *Int. J. Hydrogen Energy*, vol. 47, no. 75, pp. 31985–32003, Sep. 2022.
[55] P. Olivier, C. Bourasseau, and P. B. Bouamama, "Low-temperature electrolysis system modelling: A review," *Renew. Sustain. Energy Rev.*, vol. 78, pp. 280–300, Oct. 2017.
[56] J. Palathingal, "Mathematical modelling and dynamic simulation of a PEM electrolyser," M.S. thesis, Groupe de Recherche en Énergie Électrique de Nancy, Univ. Lorraine, Vandœuvre-lès-Nancy, France, 2017.
[57] K. S. Agbli, M. C. Péra, D. Hissel, O. Rallières, C. Turpin, and I. Doumbia, "Multiphysics simulation of a PEM electrolyser: Energetic macroscopic representation approach," *Int. J. Hydrogen Energy*, vol. 36, no. 2, pp. 1382–1398, Jan. 2011.
[58] W. Tiktak, *Heat Management of PEM Electrolysis*. Delft, The Netherlands: Delft Univ. Technology, 2019.
[59] A. Majumdar, M. Haas, I. Elliot, and S. Nazari, "Control and control-oriented modeling of PEM water electrolyzers: A review," *Int. J. Hydrogen Energy*, vol. 48, no. 79, pp. 30621–30641, Sep. 2023.
[60] S. R. F. Lala and S. Shahgaldi, "Mass and charge transport phenomena in porous transport layer for proton exchange membrane water electrolyzers: A review," *Energy Rep.*, vol. 13, pp. 162–183, Jun. 2025.
[61] A. Villagra and P. Millet, "An analysis of PEM water electrolysis cells operating at elevated current densities," *Int. J. Hydrogen Energy*, vol. 44, no. 20, pp. 9708–9717, Apr. 2019.
[62] G. Li, L. Wu, Y. Qin, X. Du, and G. Liu, "Gradient catalyst layer design towards current density homogenization in PEM water electrolyzer with serpentine flow field," *Energy Convers. Manage.*, vol. 314, Aug. 2024, Art. no. 118659.
[63] Ö. F. Selamet, M. C. Acar, M. D. Mat, and Y. Kaplan, "Effects of operating parameters on the performance of a high-pressure proton exchange membrane electrolyzer," *Int. J. Energy Res.*, vol. 37, no. 5, pp. 457–467, Apr. 2013.
[64] Á. Hernández-Gómez, V. Ramirez, D. Guilbert, and B. Saldivar, "Development of an adaptive static-dynamic electrical model based on input electrical energy for PEM water electrolysis," *Int. J. Hydrogen Energy*, vol. 45, no. 38, pp. 18817–18830, Jul. 2020.
[65] M. Koundi, H. El Fadil, Z. EL Idrissi, A. Lassioui, A. Intidam, T. Bouanou, S. Nady, and A. Rachid, "Investigation of hydrogen production system-based PEM EL: PEM EL modeling, DC/DC power converter, and controller design approaches," *Clean Technol.*, vol. 5, no. 2, pp. 531–568, Apr. 2023.
[66] J. S. Kim, J. Chen, and H. E. Garcia, "Modeling, control, and dynamic performance analysis of a reverse osmosis desalination plant integrated within hybrid energy systems," *Energy*, vol. 112, pp. 52–66, Oct. 2016.
[67] A. Joseph and V. Damodaran, "Dynamic simulation of the reverse osmosis process for seawater using LabVIEW and an analysis of the process performance," *Comput. Chem. Eng.*, vol. 121, pp. 294–305, Feb. 2019.
[68] H. T. El-Dessouky and H. M. Ettouney, *Fundamentals of Salt Water Desalination*. Amsterdam, The Netherlands: Elsevier, 2002.
[69] J. C. Crittenden, R. R. Trussell, D. W. Hand, K. J. Howe, and G. Tchobanoglous, *MWH's Water Treatment: Principles and Design*. Hoboken, NJ, USA: Wiley, 2012.
[70] X. Jin, A. Jawor, S. Kim, and E. M. V. Hoek, "Effects of feed water temperature on separation performance and organic fouling of brackish water RO membranes," *Desalination*, vol. 239, nos. 1–3, pp. 346–359, Apr. 2009.
[71] D. Gaublomme, L. Strubbe, M. Vanoppen, E. Torfs, S. Mortier, E. Cornelissen, B. De Gusseme, A. Verliefde, and I. Nopens, "A generic reverse osmosis model for full-scale operation," *Desalination*, vol. 490, Sep. 2020, Art. no. 114509.
[72] F. Z. Najdawi and K. T. Neptune, "Optimizing reverse osmosis membrane parameters through the use of the solution-diffusion model: A review," *Engineering*, vol. 14, no. 1, pp. 9–32, 2022.
[73] Z. Hadadian, S. Zahmatkesh, M. Ansari, A. Haghighi, and E. Moghimipour, "Mathematical and experimental modeling of reverse osmosis (RO) process," *Korean J. Chem. Eng.*, vol. 38, no. 2, pp. 366–379, Feb. 2021.
[74] S. Avlonitis, W. T. Hanbury, and M. B. Boudinar, "Spiral wound modules performance an analytical solution: Part II," *Desalination*, vol. 89, no. 3, pp. 227–246, Jan. 1993.
[75] K. P. Chee, K. P. Wai, C. H. Koo, and W. C. Chong, "Performance evaluation of reverse osmosis desalination pilot plants using ROSA simulation software," *E3S Web Conf.*, vol. 65, Jan. 2018, Art. no. 05022.
[76] *Green Hydrogen Cost Reduction: Scaling up Electrolysers to Meet the 1.5 °C Climate Goal*, IRENA, Masdar City, United Arab Emirates, 2020.
[77] *Global Hydrogen Review 2024*, IEA, Paris, France, 2024.
[78] R. A. Abdelsalam, M. Mohamed, H. E. Z. Farag, and E. F. El-Saadany, "Green hydrogen production plants: A techno-economic review," *Energy Convers. Manage.*, vol. 319, Nov. 2024, Art. no. 118907.
[79] A. E. Samani, A. D'Amicis, J. D. M. D. Kooning, P. Silva, and L. Vandevelde, "Grid balancing with a large-scale electrolyser providing primary reserve," *IET Renew. Power Gener.*, vol. 14, no. 16, pp. 3070–3078, 2019.
[80] R. Saulnier, K. Minnich, and P. Sturgess, *Water for the Hydrogen Economy*. Calgary, ALB, Canada: WaterSMART Solutions Ltd, 2020, p. 13.
[81] M. Ansari, M. A. Al-Obaidi, Z. Hadadian, M. Moradi, A. Haghighi, and I. M. Mujtaba, "Performance evaluation of a brackish water reverse osmosis pilot-plant desalination process under different operating conditions: Experimental study," *Cleaner Eng. Technol.*, vol. 4, Oct. 2021, Art. no. 100134.

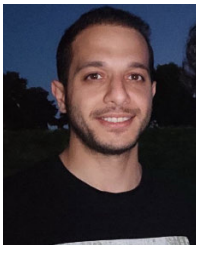

SIAVASH ASIABAN was born in Gorgan, Iran, in 1992. He received the B.Sc. degree in electrical engineering from the Ferdowsi University of Mashhad, Iran, in 2014, and the M.Sc. degree in electrical engineering from the K. N. Toosi University of Technology, Tehran, Iran, in 2017. He is currently pursuing the Ph.D. degree in electromechanical engineering with the Energy and Systems Laboratory (EnSy), Ghent University, Ghent, Belgium. His research interests include green hydrogen production technologies and the integration of renewable energy sources into power systems.

DIMITAR BOZALAKOV (Senior Member, IEEE) was born in Harmanli, Bulgaria, in 1985. He received the M.S. degree in industrial electronics from TU Varna, Varna, Bulgaria, in 2011, and the Ph.D. degree in electromechanical engineering from Ghent University, Ghent, Belgium, in 2019. Since 2019, he has been a Postdoctoral Assistant with the Energy and Systems Laboratory (EnSy), Ghent University. His current research interests include electric power systems, renewable energy applications, energy storage, improving the power quality in the distribution grids, and efficiency improvement of power electronic converters.

EMILE CORNELISSEN has been a Guest Professor in Ghent, since October 2017. He has been a Senior Scientific Researcher with the KWR Water Research Institute, The Netherlands, since 2003, and a Visiting Scientist with Singapore Membrane Technology Centre (SMTC), NTU, Singapore, since 2014. His research focuses on drinking water treatment in general and membrane filtration specifically, including topics such as membrane fouling and cleaning, rejection of emerging contaminants, forward osmosis, and developing innovative concepts. He has been active in different fields of membrane research for more than 25 years.

LIEVEN VANDEVELDE (Senior Member, IEEE) was born in Eeklo, Belgium, in 1968. He received the degree in electrical and mechanical engineering (main subject: electrical power engineering) and the Ph.D. degree from Ghent University, in 1992 and 1997, respectively. He has been with the Energy and Systems Laboratory (EnSy), Department of Electromechanical, Systems, and Metal Engineering, Ghent University. He has conducted research in various domains of electrical power engineering, inter alia, electrical machines, and (computational) electromagnetics. Since 2004, he has been a member of the professorial staff and has been coordinating the research on electric power systems at EELAB. In this research, renewable energy and its integration into electric power systems play a prominent role.